INFORMATION TO USERS

This manuscript has been reproduced from the microfilm master. UMI films the text directly from the original or copy submitted. Thus, some thesis and dissertation copies are in typewriter face, while others may be from any type of computer printer.

The quality of this reproduction is dependent upon the quality of the copy submitted. Broken or indistinct print, colored or poor quality illustrations and photographs, print bleedthrough, substandard margins, and improper alignment can adversely affect reproduction.

In the unlikely event that the author did not send UMI a complete manuscript and there are missing pages, these will be noted. Also, if unauthorized copyright material had to be removed, a note will indicate the deletion.

Oversize materials (e.g., maps, drawings, charts) are reproduced by sectioning the original, beginning at the upper left-hand corner and continuing from left to right in equal sections with small overlaps.

Photographs included in the original manuscript have been reproduced xerographically in this copy. Higher quality 6" x 9" black and white photographic prints are available for any photographs or illustrations appearing in this copy for an additional charge. Contact UMI directly to order.

Bell & Howell Information and Learning
300 North Zeeb Road, Ann Arbor, MI 48106-1346 USA
800-521-0600

UMI®

Ion Accumulation in a Paul Trap for the Canadian Penning Trap Mass Spectrometer

by

Pedro Martinez

A thesis submitted
to the Faculty of Graduate Studies and Research
in partial fulfillment of the requirements
of the degree of

Master of Science
in Physics

Foster Radiation Laboratory,
Physics Department, McGill University, Montréal, Canada.

À ma famille

Abstract

The Canadian Penning trap Mass Spectrometer (CPTMS) was reassembled and commissioned at Argonne National Laboratory. It consists of three systems: a laser desorption ion source, used for stable isotope production; a radio-frequency quadrupole ion trap (Paul trap); and a Penning trap, which sits inside a homogeneous 6 Tesla magnetic field. The CPTMS was tested using gold ions: these were accelerated toward the Paul trap, where they were accumulated and cooled down. They were then sent to the Penning trap, in which ions undergo circular motion. These motions were resonantly excited using an RF dipole electric field, and the resonant frequency was measured as a minimum in time-of-flight of the ejected ions as they were led to a region of low magnetic field, converting their cyclotron energy to axial kinetic energy. The apparatus was found to be operational: multiple-bunch accumulation was observed for the first time in a Paul trap, and the Fourier limited frequency resolution of 2×10^{-6} was attained for a one second excitation time in the Penning trap.

Résumé

Le spectromètre de masse canadien à piège de Penning a été réassemblé et mis en service au Argonne National Laboratory. L'appareil consiste en trois systèmes: une source d'ions à désorption au laser, utilisée pour la production d'isotopes stables, un piège à ions quadrupolaire à fréquence radio, aussi appelé piège de Paul, et un piège de Penning, qui réside dans un champ magnétique homogène de 6 Teslas. Ces systèmes ont été testés avec des ions d'or: ceux-ci ont été accélérés vers le piège de Paul où ils furent accumulés et refroidis, pour ensuite être envoyés au piège de Penning, dans lequel les ions décrivent un mouvement circulaire. Ces mouvements ont été excités de façon résonnante avec un champ dipolaire électrique à fréquence radio, et la fréquence de résonnance fut mesurée comme un minimum dans le temps-de-vol des ions éjectés et guidés vers une région de champ magnétique faible, ce qui convertit leur énergie cyclotron en énergie kinétique. L'appareil s'est montré opérationnel: l'accumulation de multiples paquets a été observée pour la première fois dans un piège de Paul, et la résolution Fourier-limitée de 2×10^{-6} a été atteinte pour une excitation d'une seconde dans le piège de Penning.

Contents

List of Figures

List of Tables

Acknowledgments

Mes premiers et plus sincères remerciements vont à mes parents qui m'ont donné la liberté la plus grande en m'apprenant la discipline.

Many thanks to my supervisor, professor Jonathan K.P. Lee, who gave me the chance to work on this great project. He guided me throughout the studies, the experiment, and the writing of this thesis. I thank him for the support he gave me, both academically and financially, and for the confidence he had in me.

I would also like to thank Team Trap for all that they have shown me, both in and out of the labs. From Argonne National Laboratory (ANL), to Guy Savard, for producing thought and work at such an incredible pace. The work presented in this document was done with his help and supervision. From the University of Manitoba, to Kumar Sharma, for being such a great person to learn from and learn with. He and his team provided us with the computer system and some of the electronic modules. From McGill University, to Fritz Buchinger and John Crawford, for taking the time to come to the lab and give a hand; most sincere thanks to Sid Gulick, for the help, the discussions, and the comments on the thesis. To previous members, Mike Watson and Dave Beeching, for all which is technical. To summer students, Jason Clark, Michael Ellis, Patrick Edwards-Daugherty, and Andrew Dias, for their help and friendship. To Xin Feng, for his perspicacity.

I am also eternally grateful to the people of the physics building at ANL. I can't

name all of them, but I will certainly remember all their help in setting up the apparatus. The financial support given by ANL was also greatly appreciated.

I would like to thank the people of McGill University. Steve Kekani for the machining work (and teaching), and Leo Nikkinen for the switch boxes which made the Paul trap accumulate multiple bunches. They have also made the thesis writing period more enjoyable. Thanks to the people who keep the department going, Paula Domingues, Diane Koziol, and Joanne Longo, and most of all, Jean Barrette. They were there when I needed them.

Finally, I would like to express my gratitude to the two women who have guided my studies: Mrs. Argentino and Mrs. Engelberg. I will never thank you enough for what you have seen in me.

Chapter 1

Introduction

The work presented in this document follows the initiative of a group consisting of people from the University of Manitoba, the TASCC facility of Chalk River Laboratories, and McGill University. They proposed to build a device they named the Canadian Penning Trap Mass Spectrometer, CPTMS, which would conduct high-precision mass measurements on both stable and unstable isotopes. The instrument was to be located at the TASCC accelerator site, from which the unstable species were to be obtained. Between 1994 and 1997, the apparatus was designed and assembled there. After the shutdown of the TASCC facility, the CPTMS was moved to Argonne National Laboratory, where the work described in this thesis was done.

The CPTMS was reassembled and commissioned, and the first tests of its working design were performed using laser desorption on a gold target as a stable ion source. For the first time, multiple bunches of ions were accumulated in a Paul trap. The modified cyclotron frequency of ions captured in the Penning trap was measured, and the Fourier limited resolution of 2×10^{-6} was attained for a one second excitation time.

1.1 Significance of mass values

The need for precise and accurate mass values arises principally from the field of nuclear physics, where the structure of the nucleus and the interaction between its constituent nucleons, the protons and neutrons, are studied [1]. These interactions result in a difference between the mass of a nucleus and that of the sum of its nucleons. Mass is therefore a basic property determined by all the interplaying forces which should be adequately predicted by any nuclear theory [2]. In order to develop and test such theories, mass values of high precision and accuracy have to be available for a large sample of elements.

Nuclei can be divided into two categories: the naturally occurring or stable ones, and the unstable ones. Furthermore, the unstable species lying close to the valley of beta stability form a "backbone" of well known masses [3]. Several nuclear models accurately fit the known masses of stable species. More stringent tests come from prediction of the masses of neutron-rich and neutron-deficient unstable isotopes, where particular properties of the forces involved are manifested.

There are certain aspects of the mass surface which require investigation: observation of systematic effects in long isotopic chains extending far from the valley of beta stability, the study of nuclear deformation and shell effects in the nucleus, the study of the weak interaction, breaks in the backbone at certain locations (A=20, 32, 88, 90, 105, 138)[4]. Furthermore, testing mass formulae leads to better predictions of unknown masses, existence of exotic nuclei, and estimates of the limits of nuclear stability [5]. Mass values can also be used in other areas of physics to test theories like the r-process for nucleosynthesis, and the conservation of vector current (CVC) using superallowed $0^+ \rightarrow 0^+$ beta decay reactions [6]. There is therefore a lot of work to be done in the field of mass spectrometry, and the CPTMS was designed with these physics goals in mind [4].

1.2 Previous Instruments and the CPTMS

Nuclear masses of stable nuclei have been determined traditionally using deflection type mass spectrometers [7]. For the unstable nuclei in the backbone, masses were determined from Q-values of nuclear decays and reactions. For nuclei far from stability, masses were obtained through series of Q-values linking them to the backbone. The results obtained this way were often inaccurate because of the difficulty in determining the decay schemes of the nuclei involved [8]. This also meant that errors added up as one moved away from stability [9]. Direct mass measurements for long isotopic chains are difficult because of the short lifetimes and low production yields of the radioactive species. These became available using deflection type magnetic mass spectrometers in the 70's [10, 11]. Values were later improved using time-of-flight techniques [12, 13].

The latest measurements have been made by measuring the cyclotron frequency of ions in a Penning trap [14]. The first instrument to conduct such measurements was the ISOLTRAP facility at ISOLDE at CERN [15, 16, 17]. With it, resolutions of up to 10^6 and accuracies better than 10^7 have been achieved for over 80 radionuclides [18]. ISOLDE produces radionuclei by thick-target bombardment with 1 GeV proton beams. The desired recoils are ionized and accelerated up to 60 keV, then sent to a magnetic sector isotope separator [19]. The ions are then captured by a Paul trap beam buncher, and ramped down to a few eV's. They are sent to a first Penning trap for accumulation, purification, and cooling of the ions. They are then transferred to a second Penning trap for the high precision mass measurement.

The CPTMS also measures the cyclotron frequency of ions in a Penning trap. Ions produced by laser desorption are sent to a Paul trap for multiple pulse accumulation and cooling. They are then sent to a high precision Penning trap for the mass measurement. For this work, a pulsed Nd:YAG laser was used to desorb a gold

target. The cooling in the Paul trap is achieved by introducing helium buffer gas into the trap [20]. Collisions between the He and the trapped species result in a transfer of kinetic energy and an overall cooling of the trapped species. The Penning trap is sitting inside a 6 Tesla superconducting magnet, which induces captured ions to undergo cyclotron motion. It is sectioned into quadrants. By applying an RF electric potential on them, we can drive the cyclotron motion. Ions driven at their resonant frequency will then be more energetic than the ones driven at other frequencies. When they are ejected and led to a region of low magnetic field, this cyclotron energy is converted to kinetic energy. A micro-channel plate detector is used to measure TOF as a function of driving frequency: it will show a minimum at resonant frequency.

There are two main improvements in our system: the magnet and the ion source. Our magnet is self-shielding and therefore more stable. Also, The CPTMS was designed to accept ions from an Enge spectrograph coupled to the particle accelerator of the ATLAS facility of Argonne National Laboratory. The ion beam impinges on a target, and the 0^o recoils are separated by the spectrograph before being cooled down in a gas cell and delivered through a small aperture to a linear RFQ trap. The ions collected this way are delivered to the Paul trap, and then to the Penning trap. This means that mass measurements can be made with essentially any species produced with the beam available at ATLAS. This is to be compared with the ISOLDE proton beam, which has very low yields for transuranium nuclei. As mentioned before, the ISOLDE apparatus achieved precisions of 10^{-7}. The CPTMS was designed to eliminate known systematic errors to the 10^{-8} level[4].

1.3 Outline

The thesis will be divided into three parts: first, the theory of ion traps and mass determination using them will be reviewed. Then, the CPTMS will be described.

Finally, the experiments performed will be presented along with the results. The discussion and conclusions will follow.

Chapter 2

Theory

The theory of ion trapping and high precision mass measurement using traps is reviewed. This will give us insight on both the physical mechanisms involved and the relevant parameters. We will use three coordinate systems: cartesian, with coordinates (x, y, z), polar (r, ϕ, z), and spherical (R, ϕ, θ), where ϕ and θ are the azimuthal and polar angles, respectively.

2.1 Quadrupole fields as 1-dimensional ion traps

Our goal is to confine an ion in three dimensions using electrical and magnetic fields. We start with Newton's second and Coulomb's laws for the force $\vec{F}$ on a particle of mass m and charge q:

$$\vec{F} = m\vec{a} = q\vec{E}, \qquad \vec{E} = -\nabla\Phi, \tag{2.1}$$

where $\vec{a}$ is the acceleration, $\vec{E}$ is the electric field, and Φ is the electric potential. The potential in free space is given by the Laplace equation,

$$\nabla^2\Phi = 0, \tag{2.2}$$

a solution of which can be obtained via the well known multipole expansion:

$$\Phi = \sum_{l,m} a_{lm}\Phi_{lm}, \qquad \Phi_{lm} = R^l P_l^m(\cos\theta)\cos(m\phi). \tag{2.3}$$

Here, the $P_l^{m\prime}s$ are the associated Legendre polynomials. Assuming azimuthal symmetry, we can set $m = 0$ and get an expression in terms of the normal Legendre polynomials P_l :

$$\Phi = \sum_{l} a_l\Phi_l, \qquad \Phi_l = R^l P_l(\cos\theta). \tag{2.4}$$

Let us look at the first terms in this expansion: the monopole, $l = 0$, gives us a field of zero. The dipole, $l = 1$, gives us a field $\vec{E_1} = -a_1\hat{z}$, corresponding to a constant force in the $-z$ direction. The quadrupole, $l = 2$, gives us the following:

$$a_2\Phi_2 = \frac{a_2}{2}(2z^2 - r^2) \quad \Rightarrow \quad \vec{E} = (a_2 r, 0, -2a_2 z). \tag{2.5}$$

This saddle-like potential is shown in figure 2.1. Assuming that q and $a > 0$, we see that we have a linear restoring force in the z direction but no confinement in the r plane, which is nevertheless a beginning. From the uniqueness of solutions to the Laplace equation[1], we know that defining a voltage along an equipotential surface of equation 2.5 will establish such a field. We must then place hyperbolic electrodes along an isoline, say at a characteristic distance z_o from the origin. This is shown in figure 2.2. If we set the potential along these surfaces to $\pm V_o$, we get expressions for both a_2 and the coordinates of the electrodes:

[1][21], p.42

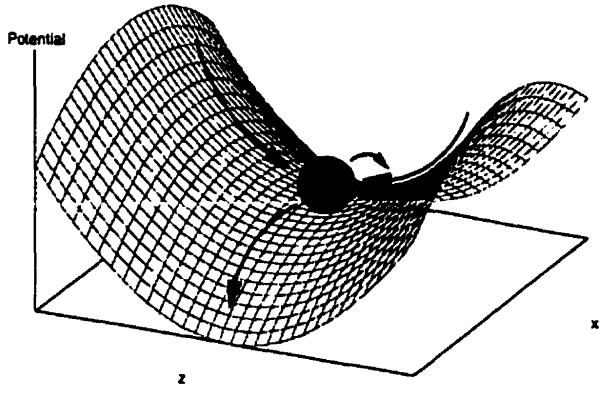

Figure 2.1: Quadrupole potential. It is plotted along a cut in the y plane.

$$a_2 = \frac{V_o}{2z_o^2} \qquad \frac{z^2}{{z_o}^2} - \frac{r^2}{\left(\sqrt{2}z_o\right)^2} = \pm 1 \tag{2.6}$$

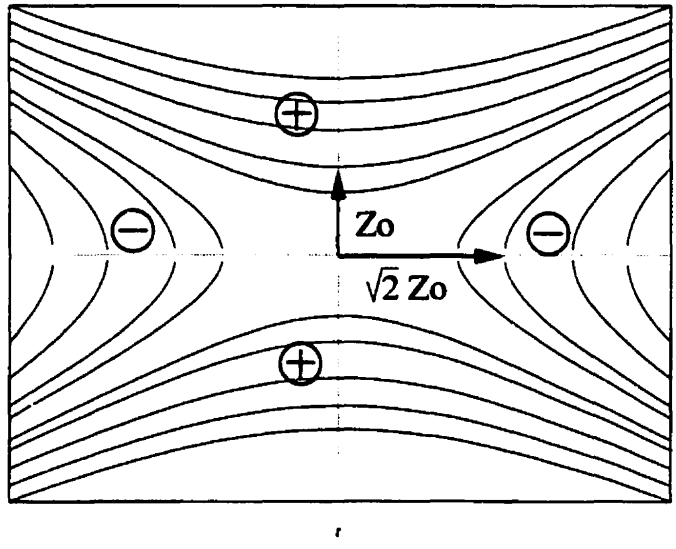

Figure 2.2: Equipotential lines for a quadrupole. Also shown is a characteristic distance z_o, defining the isoline along which the electrodes will lie.

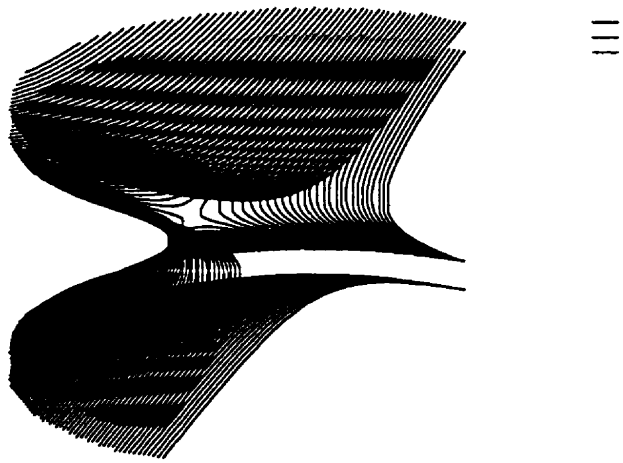

Figure 2.3: Geometry of a quadrupole trap. A cut was made along the $x = 0$ plane to show the inside.

The trap created this way will look like the one shown in figure 2.3. There, we see half of a trap, so that the inside is shown. It is made of a top and bottom endcap, and a ring. A physical trap has to be of finite extent, and this will add terms with $l \neq 2$ to the potential. Let us restrict the analysis to the ideal case. The equation of motion for a particle in an ideal quadrupole trap with DC voltages applied to the endcaps is given by equation 2.1. Using the electric field given by equations 2.5 and 2.6 and solving for the position, we get the following:

$$z(t) \propto \sin(\omega_z t) \qquad r(t) \propto e^{\pm \omega_r t}. \tag{2.7}$$

An ion in such trap would therefore undergo oscillatory motion in the axial direction at a frequency ω_z,

$$\omega_z = \sqrt{\frac{2qa_2}{m}} \equiv \sqrt{\frac{q}{m}\frac{V_o}{z_o^2}}, \tag{2.8}$$

and an unbound exponential motion in the radial direction. This is shown in two

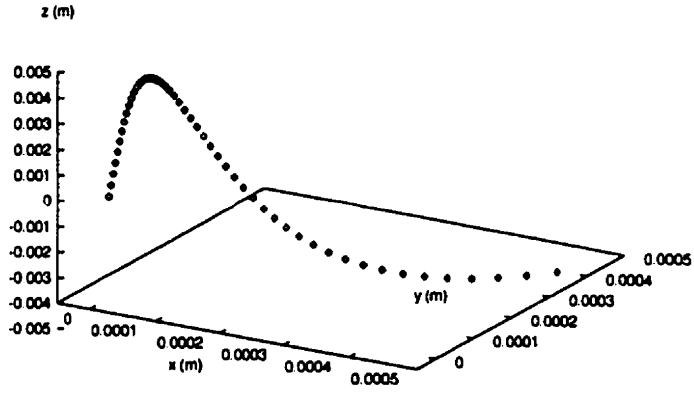

Figure 2.4: Ion in a 3-dimensional quadrupole field. This is for Au^{1+} in a $1000V$ DC starting at the origin with velocity components corresponding to $(.01, .01, 500)eV$ in kinetic energy. 50 steps in $1\mu s$.

dimensions in figure 2.4.

Now that we can trap an ion in the axial dimension, we have to devise a scheme that will allow confinement in the radial direction; the following sections show us two alternatives.

2.2 Radial confinement using AC electric fields: the Paul trap

We see from equations 2.5 and 2.6 that the sign of the potential V applied between the trap's endcaps and ring decides, along with the charge of the ion, whether the trapping will be in the axial or radial direction. By alternating the sign of V, it is possible to confine a particle in three-dimensional space; such is the principle of operation of a Paul or RFQ trap. Let us derive the equations of motion for an ion in

a Paul trap where V is a superposition of a DC and an AC part:

$$V(t) = V_{DC} + V_{AC}\cos(\omega_D t). \tag{2.9}$$

We can rewrite equation 2.1 for the force on the ion as

$$\frac{d^2u}{dt^2} - \frac{c_u}{2{z_o}^2}\frac{q}{m}\left[V_{DC} + V_{AC}\cos(\omega_D t)\right]u = 0, \tag{2.10}$$

where u is any of the x, y, z coordinates, and $c_x = c_y = 1$, $c_z = -2$. Rewriting the equation in terms of the angle ξ defined by [2]:

$$\xi \equiv \frac{\omega_D t}{2}, \tag{2.11}$$

we get:

$$\frac{d^2u}{d\xi^2} + \left[a_u - 2q_u\cos(2\xi)\right]u = 0, \tag{2.12}$$

where

$$a_u = -2\frac{c_u}{{\omega_D}^2{z_o}^2}\frac{q}{m}V_{DC}, \quad q_u = \frac{c_u}{{\omega_D}^2{z_o}^2}\frac{q}{m}V_{AC}. \tag{2.13}$$

Equation 2.12 is known as the Mathieu equation [23]. We find the solution of this second order differential equation by following the steps in [22]. It will be a linear combination of two independent solutions, say

$$u = A_1u_1(\xi) + A_2u_2(\xi). \tag{2.14}$$

Also, let us say that u_1 is an even function of ξ, and u_2 is an odd one. We look for periodic solutions:

[2] [22], p.34

$$u(\xi + \pi) = e^{\mu\pi}u(\xi), \tag{2.15}$$

with $\mu = \alpha + i\beta$, a constant. Defining the function $\phi(\xi) = e^{-\mu\xi}u(\xi)$, we see that:

$$\begin{aligned} \phi(\xi + \pi) &= e^{-\mu(\xi+\pi)}u(\xi + \pi) \\ &= e^{-\mu\xi}u(\xi) \\ &= \phi(\xi); \end{aligned} \tag{2.16}$$

ϕ is therefore a function of ξ with period π, which means that we can expand it:

$$\phi(\pm\xi) = \sum_{n=-\infty}^{\infty} c_{2n}e^{\pm i2n\xi}. \tag{2.17}$$

The general solution then becomes:

$$u(\xi) = B_1e^{\mu\xi}\sum c_{2n}e^{i2n\xi} + B_2e^{-\mu\xi}\sum c_{2n}e^{-i2n\xi}. \tag{2.18}$$

Here, B_1 and B_2 are two new constants. For the solution to be stable (i. e. bounded), we need the exponential term e^{μ} to be imaginary; we set $\alpha = 0$ and expand the complex exponentials to obtain a solution of the same form as 2.14:

$$u(\xi) = A_1\sum_n c_{2n}\cos[(2n + \beta)\xi] + A_2\sum_n c_{2n}\sin[(2n + \beta)\xi]. \tag{2.19}$$

The c_{2n}'s are defined recursively using the formula[3]:

$$\frac{c_{2n}}{c_{2n-2}} = \frac{-q}{(2n+\beta)^2\left(1 - \frac{a}{(2n+\beta)^2} - \frac{q^2}{(2n+\beta)^2(2n+2+\beta)^2(1-\ldots)}\right)}. \tag{2.20}$$

[3][22], p.72

We normalize using $c_0 = 1$. The stability and boundedness of this solution depends on the values of a_u and q_u. This can be seen by expressing β as a function of these parameters[4]:

$$\beta^2 = a + \cfrac{q^2}{(2+\beta)^2 - a - \cfrac{q^2}{(4+\beta)^2 - a - \cfrac{q^2}{(6+\beta)^2 - a - \cdots}}} + \cfrac{q^2}{(\beta-2)^2 - a - \cfrac{q^2}{(\beta-4)^2 - a - \cfrac{q^2}{(\beta-6)^2 - a - \cdots}}}. \quad (2.21)$$

Using this equation, we can divide the $a-q$ plane into stable and unstable regions, as shown in figure 2.5. This diagram was produced by taking (a,q) pairs and plugging in to equation 2.21. If the expression converged to a finite value, then the point was taken as being stable. Note that the diagram is symmetric about the a axis, but not about the q axis.

Since a and q are proportional to the DC and AC components of the voltage, Paul traps are normally operated in the island of stability closest to the origin, where the potentials are smallest and easiest to produce; we therefore take a closer look at that part of the diagram and look at iso-β lines; this is shown in figure 2.6.

There, we show two superposed stability diagrams: one for the radial motion (the top one), and one for the axial motion (the bottom one). Remember that there is a factor of -2 between the two. This means that stable trajectories in all dimensions are possible for the conditions corresponding to the intersection of the two plots.

Using this, we can depict the motion of a captured ion. An example is shown in figure 2.7. We can see a complex superposition of oscillations; let us look at the x-motion, shown in figure 2.8. There, we show three plots: the actual motion of the ion as a function of time, and the two main components of the motion (on an

[4][22], p. 72

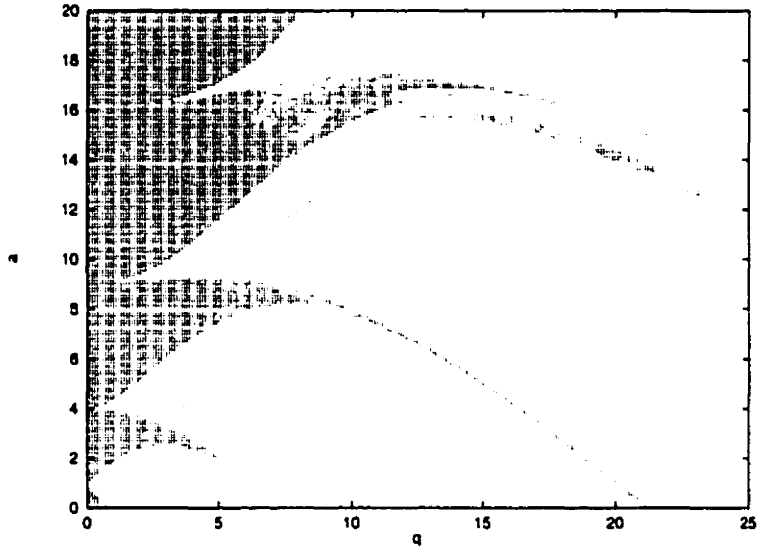

Figure 2.5: Stability diagram for the Mathieu equation (also called a Mathieu diagram). Each point represents an (a,q) pair for which equation 2.21 converges. Note that the diagram is symmetric about the a axis, but not about the q axis.

arbitrary scale, to make things more understandable). The motion is made up of a fundamental motion called *secular* motion of frequency $\omega_o = \beta\frac{\omega_D}{2}$ and higher-order ones (ω_n). The corresponding frequencies can be obtained from equations 2.11 and 2.19:

$$\omega_n = (2n + \beta)\frac{\omega_D}{2}.$$

2.3 Radial confinement using magnetic fields: the Penning trap

As a second alternative for radial confinement, we look at the force on an ion in a region of free space with a homogeneous magnetic field $\vec{B} = B\hat{z}$, as given by (part of) the Lorentz formula:

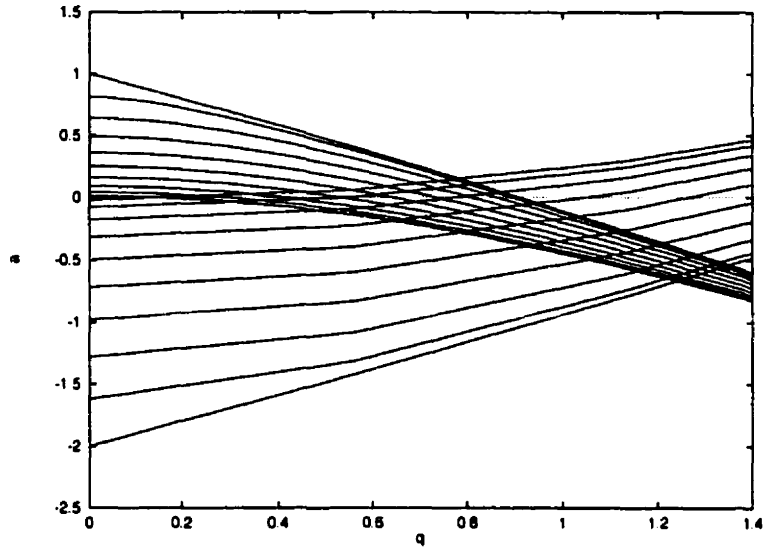

Figure 2.6: Iso-β lines for the first island of stability in the Mathieu diagram. Two plots are superposed: the top one is for the radial motion, and the bottom one is for the axial motion. Stable trajectories correspond to the area of intersection of the two plots. For each plot, from top to bottom, starting with $\beta = 1.0$ in steps of -0.1.

$$\vec{F} = q(\vec{v} \times \vec{B}), \tag{2.22}$$

where $\vec{v}$ is the velocity of the ion. The solution,

$$r(t) = r(0), \qquad \phi(t) = \omega_c t, \qquad z(t) = z(0) + \dot{z}t, \tag{2.23}$$

involves the expected cyclotron motion at a frequency ω_c given by:

$$\omega_c = \frac{q}{m} B. \tag{2.24}$$

This motion is exemplified in figure 2.9. Using a quadrupole DC electric field for axial confinement and a homogeneous DC magnetic field, we should be able to confine an ion in three- dimensional space; such is the principle of operation of a Penning trap. If the electric field had no radial component, we would expect harmonic oscillations

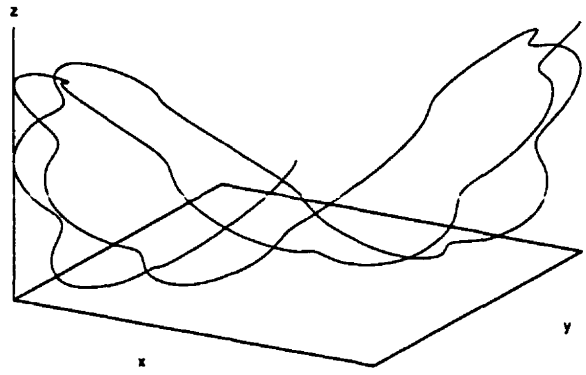

Figure 2.7: Ion motion for an Au ion in a Paul trap. This is for our geometry, with no buffer gas cooling, and an AC voltage of 400V at 350kHz. The trajectory is shown for 50μs.

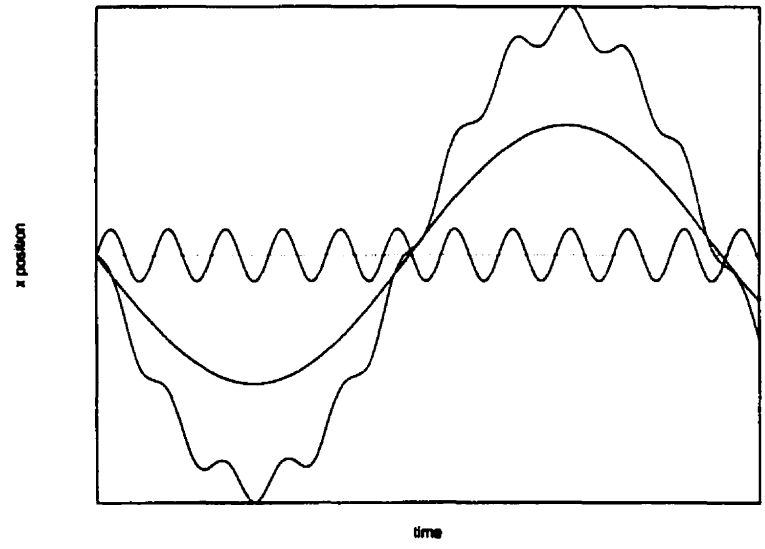

Figure 2.8: x motion for an Au ion in a Paul trap. This is for the same settings as that of figure 2.7, for the first 30μs. Also shown are the two main frequency components which make up the motion.

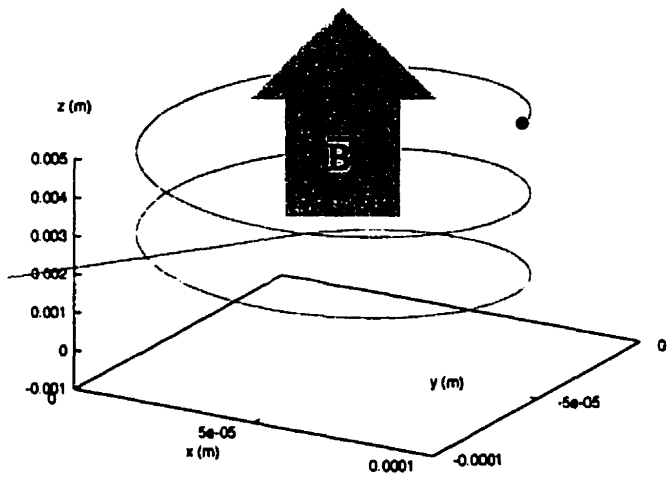

Figure 2.9: Ion in a DC magnetic field. This is for Au^{+1} in a $6T$ field starting at the origin with $(.01, .01, 1)eV$ kinetic energy; the field is on for $5\mu s$.

in the $\hat{z}$ direction and an independent cyclotron motion in the xy plane. However, the $a_2 r\hat{r}$ component of the electric field will modify the motion. The axial equation of motion will remain the same as in equation 2.23. We assume $\vec{B} = -B\hat{z}$ and write the Lorentz formula for the radial component of the force:

$$\vec{F}_r = m\ddot{\vec{r}} = q(\dot{\vec{r}} \times \vec{B} + \vec{E}_r) = q\left[B(\hat{z} \times \dot{\vec{r}}) + a_2\vec{r}\right]. \tag{2.25}$$

In order to solve this, we look at the $\hat{y}$ part of the equation, which can be written in the following way:

$$\ddot{y} - \omega_c\dot{x} - \frac{\omega_z^2}{2}y = 0. \tag{2.26}$$

We note that this equation is a quadratic in time derivatives; we expect its solution to involve the solutions to the associated quadratic equation

$$\omega^2 - \omega_c\omega - \frac{\omega_z^2}{2} = 0, \tag{2.27}$$

given by the two frequencies:

$$\omega_{\pm} = \frac{\omega_c}{2} \pm \sqrt{\left(\frac{\omega_c}{2}\right)^2 - \frac{{\omega_z}^2}{2}}. \tag{2.28}$$

In order to find the complete solution, we introduce two vectors $\vec{V}^+$ and $\vec{V}^-$[5]:

$$\vec{V}^{\pm} = \vec{r} - \omega_{\mp}(\hat{z} \times \vec{r}). \tag{2.29}$$

These two velocity vectors rotate at frequencies $\omega_{\pm}$. Using them, the equations of motion can be rewritten as

$$\dot{\vec{V}}^{\pm} = \omega_{\pm}(\hat{z} \times \vec{V}^{\pm}), \tag{2.30}$$

which are those of two-dimensional simple harmonic oscillators:

$$\vec{V}^{\pm}(t) = V_{\pm}\cos(\omega_{\pm}t)\hat{x} + V_{\pm}\sin(\omega_{\pm}t)\hat{y}, \tag{2.31}$$

where $V_{\pm}$ are amplitudes. We see that $\vec{V}^{\pm}$ rotate at frequencies $\omega_{\pm}$. We can go back to cylindrical coordinates using:

$$\vec{r} = \frac{-\hat{z} \times (\vec{V}^+ - \vec{V}^-)}{\omega_+ - \omega_-}. \tag{2.32}$$

The radial ion motion is thus a superposition of two circular motions: one slow precession at a frequency ω_-, the *magnetron motion*, and a fast motion of frequency ω_+, the *modified cyclotron motion*. A typical ion path can be seen in figure 2.10. This is for a gold ion, which has $\frac{\omega_c}{2\pi} \approx 1MHz$. To get an idea of the ratio between the frequencies, in this 5V trap, $\omega_+ \approx \omega_c$, $\omega_- \approx \frac{\omega_c}{1000}$, and $\omega_z \approx \frac{\omega_c}{10}$.

[5][24], p. 239

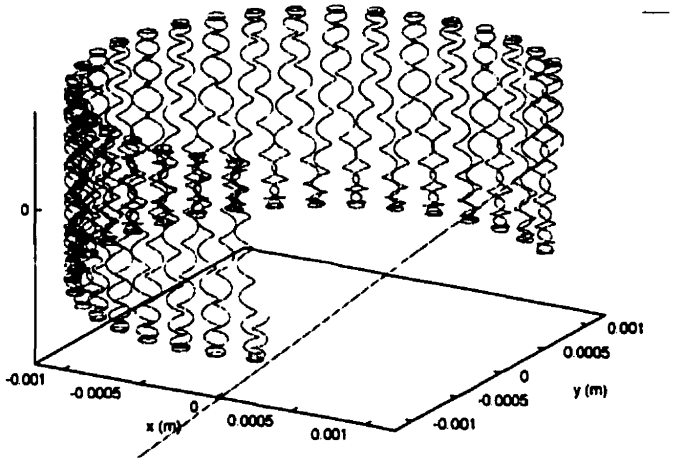

Figure 2.10: Ion motion in a Penning trap. This is for Au^{+1} in a 6T field with $5V$ bias with initial initial position $(1,1,1)mm$ and kinetic energy $(.01,.01,1)eV$. The field is on for $1ms$.

2.4 Mass measurement with a Penning trap: dipole excitation

Looking back at expression 2.24 for the cyclotron frequency of an ion in a magnetic field, we see that knowledge of B, q, and ω_c gives us the mass of the trapped ion. In the last section, though, we saw that once an ion is captured in a Penning trap, its motion involves the frequencies ω_+ and ω_-. We can also use these parameters to obtain the ion's mass since $\omega_\pm$ are functions of ω_c and ω_z. In particular:

$$\omega_+ + \omega_- = \omega_c. \tag{2.33}$$

We can determine these frequencies experimentally by exciting the resonances of the ions in the trap. Let us use an RF azimuthal dipole field at a frequency ω_D (this can be set by splitting the trap's ring into two halves, and applying an AC voltage

between them [25]). We drive the ions with an electric field given by

$$E_D = E\sin(\omega_D t)\hat{x}. \tag{2.34}$$

The new solution for $\vec{r}$ is given by the following:

$$\vec{r}_D = \frac{1}{\omega_+ - \omega_-}\left[(V_{Dy}^+ - V_{Dy}^-)\hat{x} - (V_{Dx}^+ - V_{Dx}^-)\hat{y}\right]. \tag{2.35}$$

In this case, $\vec{V}^\pm$ are also functions of ω_D:

$$\vec{V}_D^\pm = \vec{V}^\pm + \alpha_\pm\omega_D\cos(\omega_D t)\hat{x} + \alpha_\pm\omega_\pm\sin(\omega_D t)\hat{y}, \tag{2.36}$$

$$\alpha_\pm = \frac{qE}{m}\frac{1}{\omega_\pm^2 - \omega_D^2}. \tag{2.37}$$

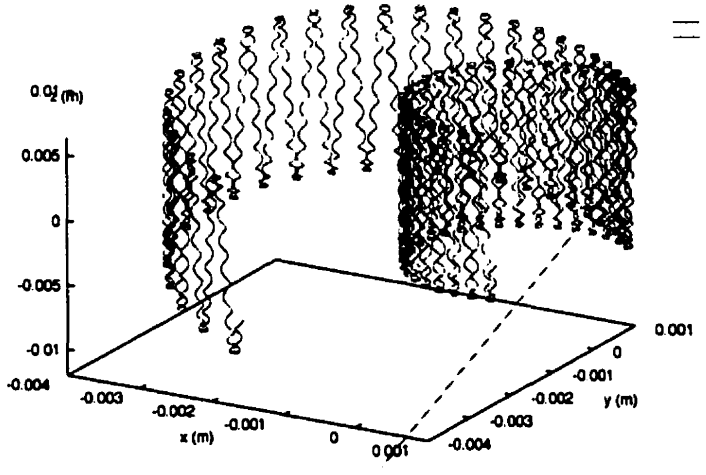

Figure 2.11: Dipole excitation for an ion in a Penning trap. Trajectories are shown for both the conditions of figure 2.10 and for an added dipole field of $50V/m$ @ $\omega_D = .96\omega_-$.

This shows us that the amplitude of the motion will increase when ω_D approaches a resonant frequency — note that this will occur only at frequencies $\omega_\pm$, not at ω_c.

This is shown in figure 2.11. There, we see two ions: one is the same as in figure 2.10 (the smaller-radius magnetron motion), and the other is driven close to ω_-; the effect is that the magnetron motion is amplified. In the same way, by driving close to ω_+, the modified cyclotron motion would be amplified. By devising a scheme for detecting these resonances at $\omega_\pm$, we can therefore deduce the mass.

2.5 Time-of-flight for the determination of cyclotron frequencies

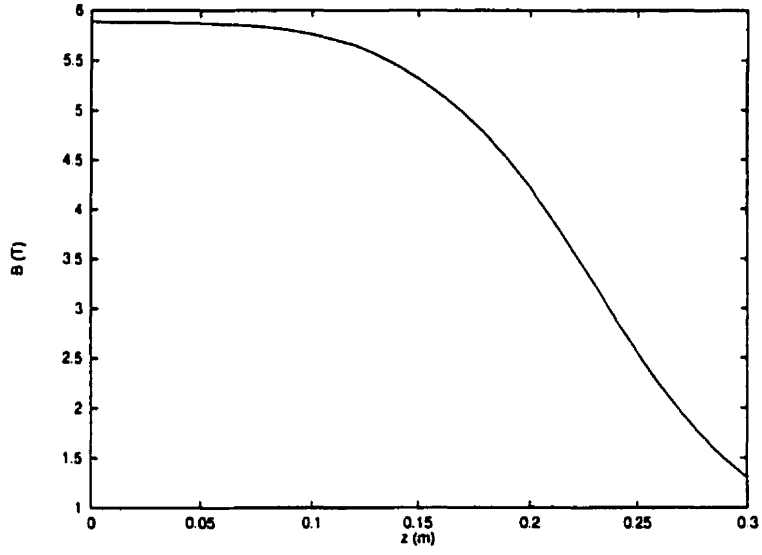

Figure 2.12: Magnetic field along the axis of the magnet.

Resonant excitation as described in the previous section results in a high cyclotron energy for ions having been driven at resonant frequency. One way to detect this energy increase is by ejecting the ions out of the Penning trap and leading them to a region of lower magnetic field. The cyclotron energy is converted to axial kinetic energy. The magnetic field above the Penning trap is shown in figure 2.12: we see that the field is homogeneous around the trap, and then falls quadratically. The

effect of the magnetic field gradient on the ion's motion is shown in figure 2.13.

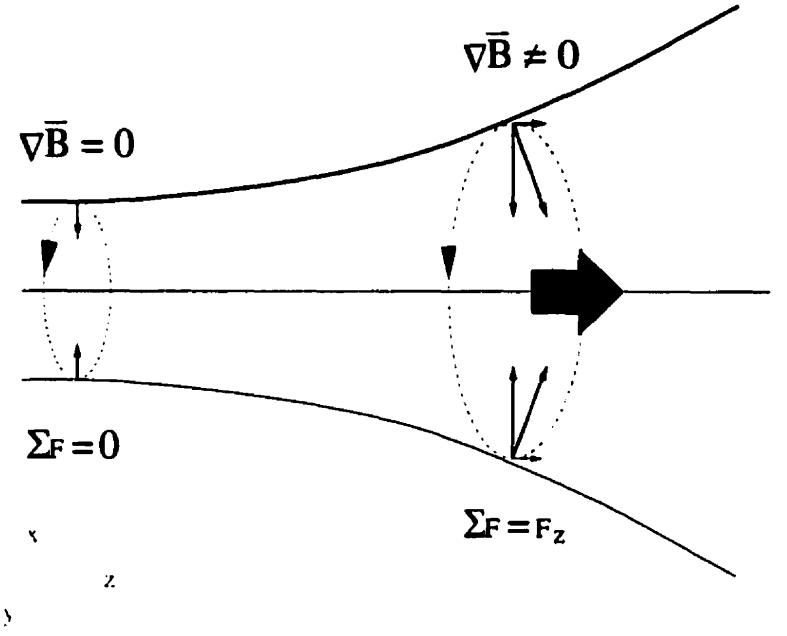

Figure 2.13: Conversion from cyclotron to axial kinetic energy.

The time-of-flight will therefore become shorter as ω_D approaches ω_+. One should remember, though, that we have derived the equations of motion for an infinite sine wave. Since we have to apply $\vec{E}$ for a finite time, say t_D, then what the ion sees is in fact an infinite series of sine waves of different frequencies given by its Fourier expansion. It was shown that this results in a limit in resolution of $\frac{1}{T_D}$ [6], as shown in figure 2.14. This is a very important result in that it shows us the theoretical limit in resolution of our measurements: a one second dipole excitation can give at best a $1Hz$ resolution. We call this the Fourier limit of the measurement.

[6][25], p. 4364

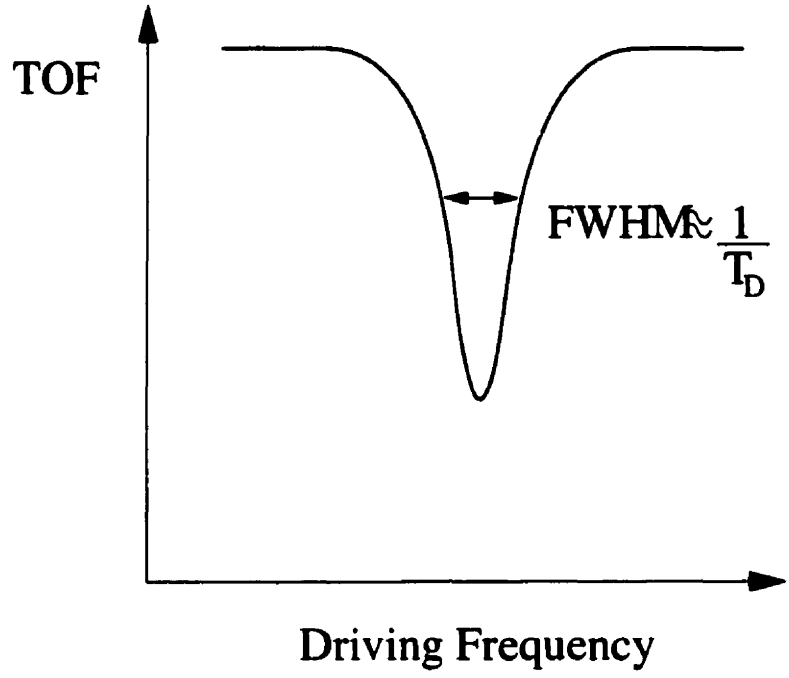

Figure 2.14: Expected TOF spectrum. The full width at half-maximum, FWHM, corresponds to the precision of the measurement.

2.6 Multiple bunch accumulation in the Paul trap

The CPTMS was designed to conduct mass measurements on both stable and unstable isotopes. One challenge in such experiments with radioisotopes is in coping with the low production yields of the desired species. The CPTMS solves this problem through multiple bunch accumulation in the Paul trap; a sufficient number of ions can be selectively stored and cooled in it before being transferred to the Penning trap.

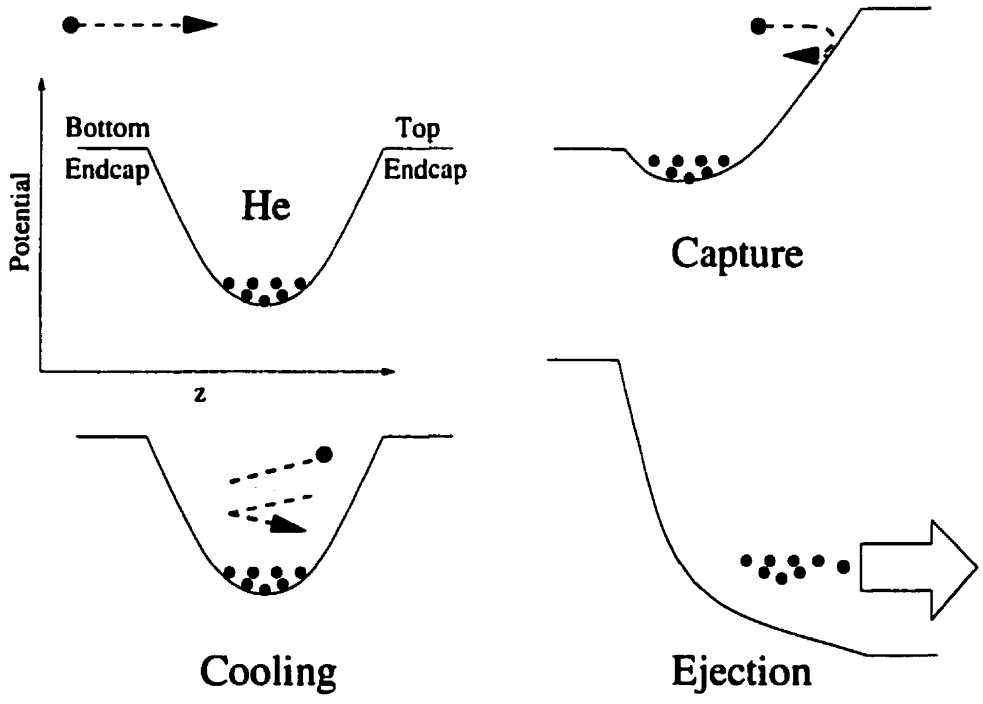

Figure 2.15: Multiple bunch accumulation in the Paul trap.

The method is depicted for one ion in figure 2.15: the trap's top endcap is pulsed as the ion approaches it. The ion slows down, and before it is reflected back, the endcap is pulsed back to its original potential. In this way, the ion is stopped inside the trap with low energy, is captured, and can be cooled down via collisions with the buffer gas. Since the ions which were already in the trap have been cooled, they have

less energy than the newly captured ion and therefore don't have time to escape.

One could argue that a Penning trap could be used for ion bunching and cooling. The high-precision Penning trap needs to operate under ultra-high vacuum. Because of this, it can't be used to cool down ions (at least not with buffer gas). Furthermore, only low voltages (a few tens of volts at the most) can be applied to it without discharges occurring (remember that we are sitting inside a high magnetic field). Since ions arriving at the trap will have typical energies of at least a few hundred electron-volts, it would be quite difficult to capture them with the scheme described above.

Chapter 3

The CPTMS

The CPTMS as used for stable isotope mass measurements is presented. First, an overview of the system is given. Then, each of its parts is described, following the ion trajectory in a mass measurement process. Finally, its control systems are reviewed.

3.1 General setup

A schematic diagram of the CPTMS is shown in figure 3.1: its main components are the laser desorption ion source, the Paul trap , the Penning trap —which sits inside a 6T superconducting magnet, and the time-of-flight (TOF) detector. Ions produced at the sample wheel via laser desorption are accelerated toward the Paul trap (also called a RFQ trap) for capture, accumulation, and cooling via collisions with high purity helium buffer gas. They are then ejected and sent to the Penning trap to be once again captured and resonantly excited. They are finally ejected and pulled towards the TOF detector, yielding a TOF spectrum. As described in section 2.4, the cyclotron energy of the ions will increase as they are driven at frequencies ω_D closer to the resonant ones. Once pulled out of the magnetic field, this cyclotron energy will convert to axial kinetic energy, giving a shorter TOF. We can therefore repeat

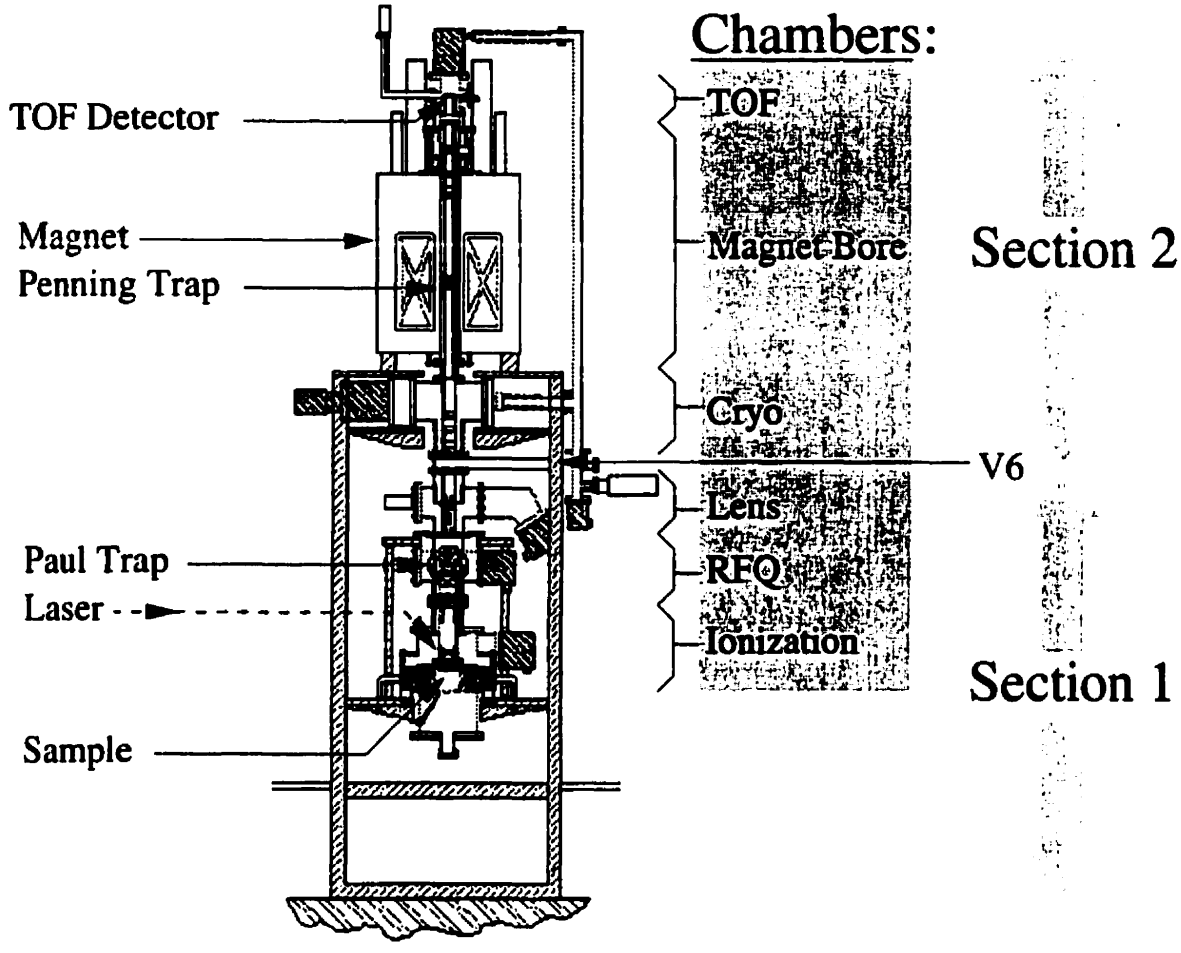

Figure 3.1: The CPTMS and its main components.

the above process for different ω_D's and plot average TOF vs ω_D; the plot will look like the one in figure 2.14, with a minimum at the resonant frequency. From this, we can get a mass value through equations 2.24, 2.28, and 2.33.

The components of the CPTMS and the electrodes which guide the ions in their path are housed inside stainless steel vacuum chambers; the 4.6m tall setup is held vertically by a square-based tower. Figure 3.1 also shows the nomenclature for the main parts, as it will be used in the following description. The apparatus is separated

into two sections by a vacuum valve, V6: this enabled the operation and testing of the ion source and Paul trap while the top section was being assembled.

We will describe the apparatus by following the path of the ions through it, starting from their production (bottom) to their final TOF detection (top).

3.2 Ion source and injection into the Paul trap

The method we chose to produce stable ions is laser desorption: we direct a high power laser at a target, and the heat deposited induces some of the material into leaving the substrate as positive ions.

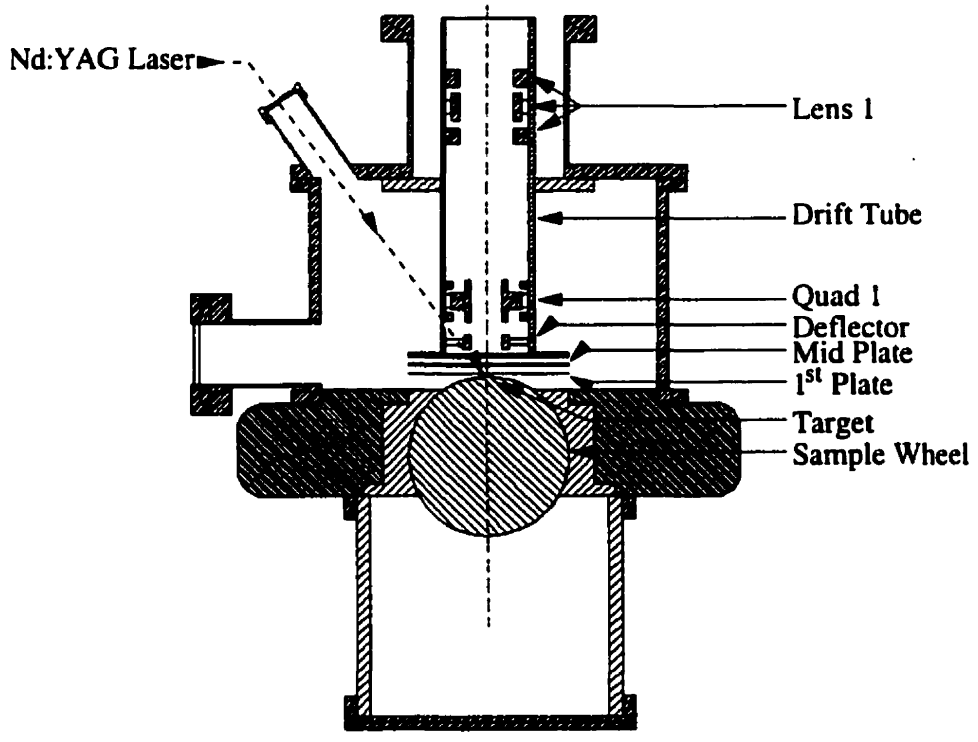

Figure 3.2: Ionization chamber [top]. Also shown are the sample wheel and the plexiglass chamber [bottom].

A schematic diagram of the ionization chamber, where the ions are produced, is

Electrode	Voltage (V)
Sample Wheel	-285
1^{st} Plate	-985
Mid Plate	-1235
Drift Tube	-1235
Lens 1	-440

Table 3.1: Typical potentials in the Ionization Chamber. The Deflector is sitting at drift potential.

shown in figure 3.2: we can see the sample wheel, which contains the target. The laser is sent from the outside through a window and focused on it; the ions produced are accelerated upward by applying potentials on the two plates and the drift tube which holds the electrodes. The quad ring, Quad 1, is used to steer the beam. The Einzel lens, Lens 1, is used to focus it at the entrance of the Paul trap. Table 3.1 shows typical potentials applied to these electrodes.

Lens 1 is made of three consecutive annular electrodes: the first and last ones are set at drift potential, and the middle one is set at a different voltage to focus our positive ions, as shown in figure 3.3. This figure, along with the rest of the ion optical simulations shown in this thesis, was produced using SIMION 3D 6.0 [26]. On the left, it shows a cut through an Einzel lens, along with the trajectory of ions flying through. On the right, we can see the potential plotted along the same plane. Quad 1 is made of one annular electrode, segmented into quarters. It is biased at drift potential, and opposite electrodes are offset by equal and opposite voltages to steer positive ions toward the one with the lowest potential. Figure 3.4 shows this in a two-dimensional geometry; once again, we see the geometry on the left, and the potential on the right.

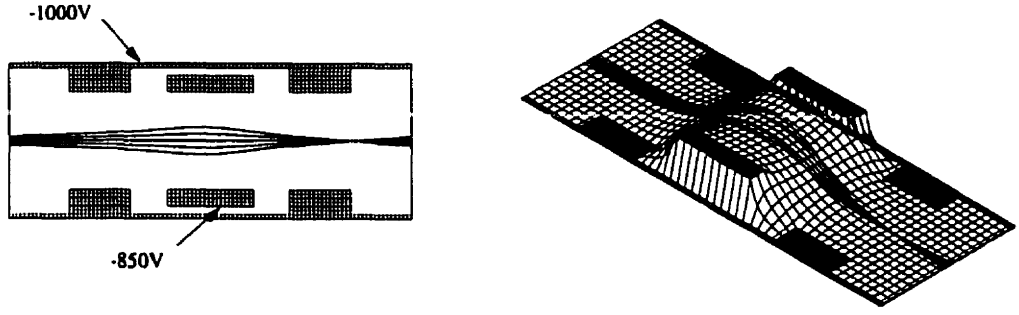

Figure 3.3: Geometry (left) and electric potential (right) for an Einzel lens, along with the trajectory for 5 ions. The electrodes are cylindrically symmetrical.

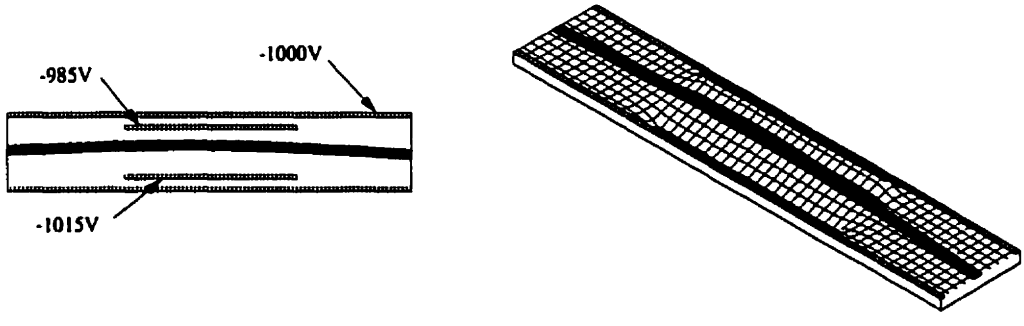

Figure 3.4: Geometry (left) and electric potential (right) for a quad ring, along with the trajectory for 5 ions. This is a two-dimensional simulation; an actual quad ring steers along two orthogonal planes. We see the effect of a 30V bias on the ring.

For the initial tests, the target used was gold: it was pressed in a tapped plug which could be screwed onto the sample wheel. The chamber at the bottom can be opened for installing a target, and then the sample wheel can be rotated to expose it to the laser beam.

A 5ns pulsed Nd:YAG laser of wavelength 532nm was used at a repetition rate of 20Hz for desorption. A polarizer was added in the path for intensity control, and the laser beam was focused using a lens with a focal length of 30.5 cm. The power used ranged between 6mJ and 10mJ per pulse.

Particles thus obtained are typically a mix of the neutral atoms and ions of the target material, the substrate, and impurities in different charge states; we can select the mass and charge we want by capturing only ions with a certain time-of-flight in the Paul trap. Production yields are quite good, although the energy distribution of the ions produced could vary with the laser beam energy and the condition of the surface of the target. In our case, we need a reasonable number of singly charged ions to be accelerated toward the Paul trap. Since the ions are to be cooled there, their initial energy distribution is not important, as long as they can get to the trap and be captured: the cooling process inside the trap eliminates the dependence on conditions at the production spot, so that the equations of motion then depend only on the conditions inside the Paul trap. Laser desorption was therefore deemed to be a suitable way of obtaining the stable isotopes needed for the first tests of the CPTMS.

Our gold target produced few contaminants, so that the capture pulse on the Paul trap was enough to select the ions we wanted. Under other circumstances, it may be necessary to have a more selective ion source. The CPTMS also provides for resonant ionization and mass-selective deflection of the desorbed species; these features were not used in our experiment.

The ions then move toward the RFQ chamber, as shown in figure 3.5. There, they

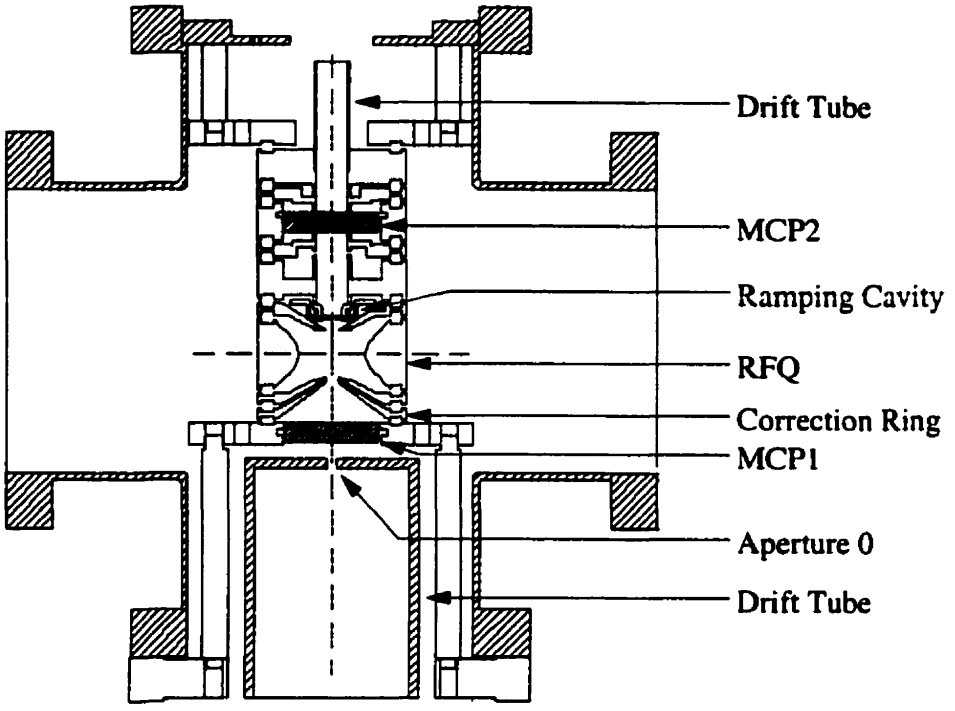

Figure 3.5: The RFQ chamber.

pass through a 3mm aperture (Aperture 0) before entering the Paul trap. Aperture 0 is installed at this position to allow a pressure differential between the RFQ chamber and the Ionization chamber. In the present setup, the ionization chamber operates at a base pressure of 1×10^{-7}torr, but as we have mentioned before, high purity helium gas is introduced into the Paul trap to cool the trapped ions. The helium pressure in the trap is about 10^{-4}torr. An aperture is necessary to allow the other sections of the spectrometer to operate at a much lower pressure. Two additional apertures are found further along the ion beam path. They have the same vacuum isolation function, and will be discussed later.

The diagram also shows two ion detectors, MCP1 and MCP2. They give a signal proportional to the number of ions impinging on their surface. They are mounted on plungers which allow them to move in or out of the ion path; once pulled out, they

are replaced by a section of drift tube. MCP1 is placed in front of the Paul trap. It is used to monitor the arrival time and intensity of the ions from the source.

3.3 The Paul trap

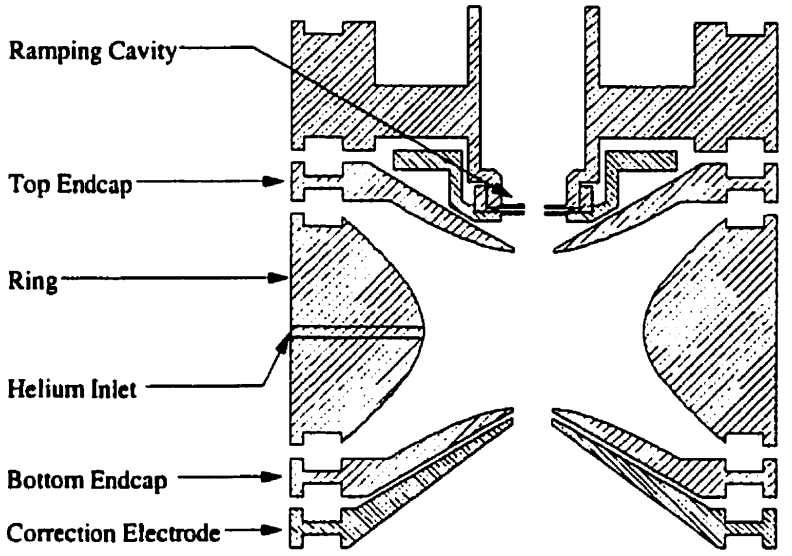

Figure 3.6: The Paul Trap. Also shown are the ramping cavity and the correction electrode.

We now come to the Paul trap, which is shown in figure 3.6. Its main structure consists of a central ring electrode and two endcaps —this is to be compared with figure 2.3. The helium buffer gas necessary for its operation is introduced into the trap cavity through an inlet on the ring electrode. The trap has a characteristic distance $z_o = 1.20$cm (see equation 2.6), corresponding to an endcap separation of 2.40cm and a ring diameter of 3.39cm. The endcaps contain holes with a diameter of 0.6cm to allow the ions to enter and leave the trap structure. The trap is preceded by a correction ring, and followed by a ramping cavity. Because of the hole on the endcap, the quadrupole field created by the trap's electrodes is affected by the drift

Electrode	Voltage (V)
MCP1 Drift Tube	-1000
Correction	-440
Paul Trap DC	-310
Top Endcap Capture	+15
Top Endcap Eject	-510
Bottom Endcap Eject	-210
Correction Cavity DC	-250
MCP2 Drift Tube	-1435
Top Drift Tube	-2235

Table 3.2: Typical potentials in the RFQ Chamber. The detectors are pulled out and replaced by sections of drift tube.

potential from the previous electrodes; the correction electrode is added at the entry and its potential is set at an intermediate value to minimize this effect.

Ions enter through the correction ring and bottom endcap, and are slowed down by a capture pulse applied to the top endcap. They are captured in the trap and cooled through collisions with helium gas. Many such ion pulses can be accumulated. Then, ejection pulses are applied on the endcaps with the bottom endcap pushing and the top one pulling the ions out of the trap. They then go through the ramping cavity where some energy correction is applied to the ions before they move on to a drift section. This results in a narrower energy distribution of the ejected ions. Table 3.2 shows typical potentials which were used in the operation of the RFQ Chamber.

The capture and ejection schemes need some further explanation. We know from section 3.3 that we have to apply a RF potential between the endcaps and the ring. We also chose not to apply any DC potential between them, which sets $a = 0$ in

equation 2.13. This means that by varying frequency of the RF applied, we can store ions of different mass ranges.It was also mentioned that we need to apply pulses for capture and ejection. Figure 3.7 shows the circuitry which does all of this: an RF signal from a waveform generator is amplified and sent through a transformer before being added to a DC bias. This signal is sent to the ring. The endcaps are connected to fast switches (20ns) which go between DC bias and capture and ejection pulse bias. Note that the top endcap has to be switched between three voltages, which is why it is connected to two switches, protected by diodes.

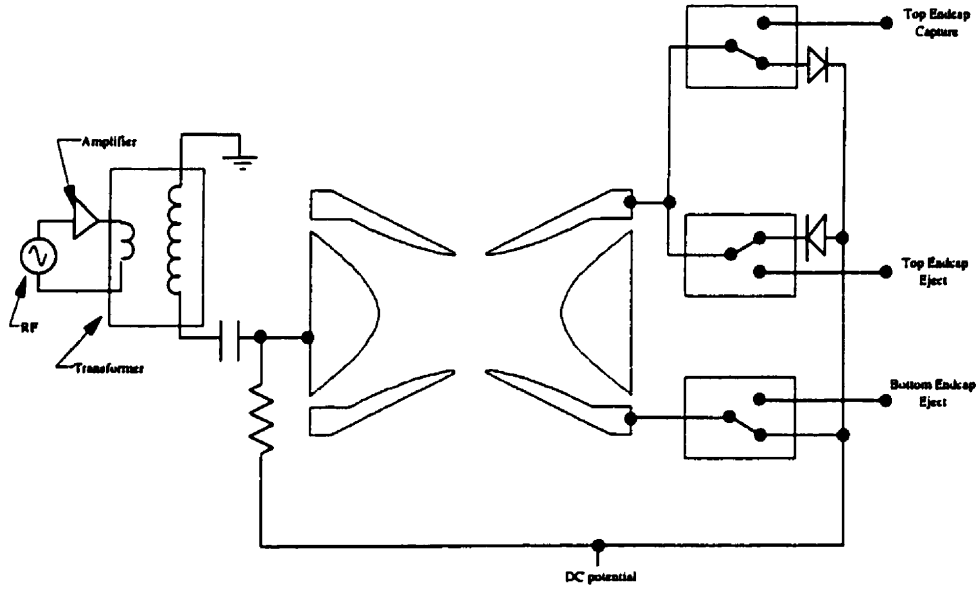

Figure 3.7: RFQ circuitry. The RF is applied to the ring. The switches are set for cooling; for capture and ejection, they are switched to the appropriate biases.

The ramping cavity was introduced at the exit of the trap to correct for the energy spread of the extracted ions: first, the magnitude of the axial quadrupole electric field is proportional to the distance from the center of the trap, as seen from equation 2.5. Since the ion cloud is of finite extent in the trap, the ejected ions will have a corresponding energy spread. Second, the RF applied to the trap means that ions ejected at different times will see a different ring potential, which also introduces

a spread in energy. A time-varying potential can be applied to the ramping cavity to compensate for this energy spread. Simulations of the ion motion show that the ions coming out of the trap first have lower energy than later ones; this means that the correction cavity has to produce a potential which accelerates the first ions more than the later ones. This is accomplished by using an arbitrary waveform generator coupled to a fast amplifier, custom-made for this purpose.

3.4 Magnet matching and injection into the Penning trap

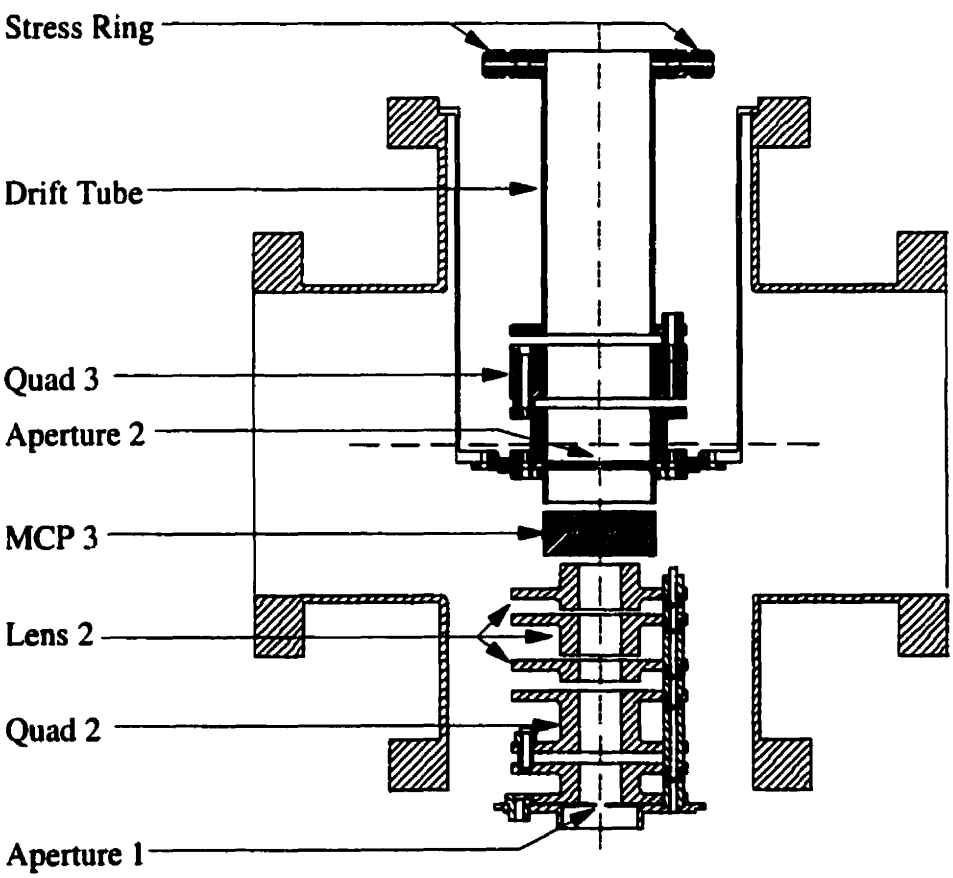

Figure 3.8: Lens chamber.

We then come to the Lens chamber, shown in figure 3.8. We saw that ions leaving the ramping cavity have the same kinetic energy. Their trajectories are then controlled such that they will enter the Penning trap along the magnetic field lines. In addition, since the Penning trap is being operated under ultra-high vacuum ($5 \times 10^{-10} torr$), adequate vacuum isolation must be provided. In the CPTMS, this appears as two apertures. Ions are first focused at Aperture 1, then steered by Quad 2, and refocused by Lens 2 to go through Aperture 2 and enter the Magnet Bore. A mobile detector, MCP3, is placed just before Aperture 2 to monitor the ions after their passage through Aperture 1. The next group of electrodes is provided to match the ion trajectory with the magnetic field lines and bring them as close to the center of the Penning trap as possible. It consists of Quad 3 (in the Lens chamber) and Quad 4 and Lens 3 (in the Cryo chamber), as shown on figure 3.9. Table 3.3 shows typical voltages on the electrodes in these chambers. Here, Quad 3 and Quad 4 were used as lenses as well as steerers.

In this injection region, the magnetic field looks like a bottleneck (see figure 2.12). Ions injected from the bottom will be fed to the magnetic field and converge toward the center of the trap as they follow the field lines. It is imperative for the ion trajectories to be parallel to the field lines. Otherwise, an excessive portion of their kinetic energy would be converted to cyclotron motion and the ions would be reflected before they get to the trap or they would arrive at the trap with an energy spread which would broaden the resonance.

It was mentioned before that these two chambers are separated by a vacuum valve, V6. During normal operation, this valve is open. This creates a region where there are no electrodes to set the electric field. The stress rings shown on the figures were added on both sides of the valve. By setting them at a higher absolute potential, they can compensate for the gap between the two drift tubes and produce a more uniform axial field. Figure 3.10 shows their effect on the electric potential. The movable

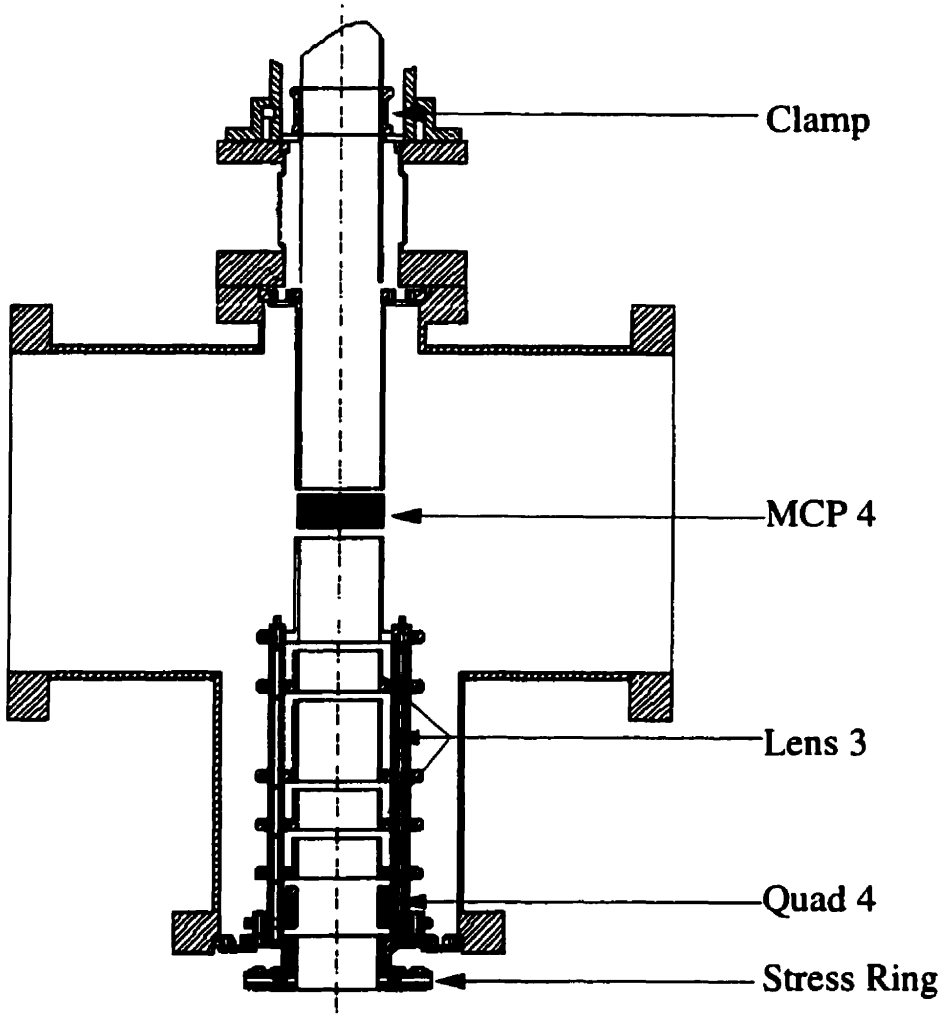

Figure 3.9: Cryo chamber.

MCP4 is placed in the Cryo Chamber, before the entrance to the magnetic bore.

3.5 The Penning trap

The ions then need to move to the Penning trap. They enter the bore of the magnet, which is shown in figure 3.11. The details of the Penning trap are shown in figure 3.12. The ions cruise inside the drift tube and are slowed down by the Deceleration

Electrode	Voltage (V)
Drift Tubes	-2235
Lens 2	-750
V6 Stress Ring	-2500
Quad 3, Quad 4 DC	-1250
Lens 3	-1100

Table 3.3: Typical potentials in the Lens and Cryo Chambers. Note the bias on the steerers: it was found that we needed to use them as lenses.

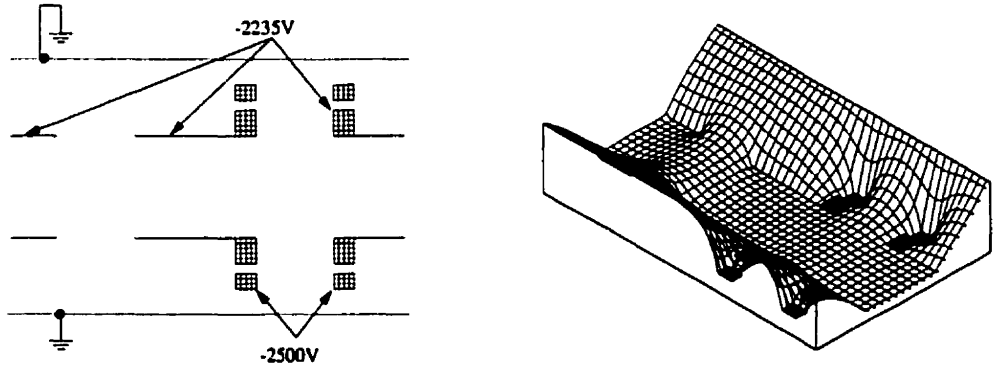

Figure 3.10: Geometry (left) and electric potential (right) for the stress ring. The electrodes are cylindrically symmetrical. A gap without stress ring is shown for comparison; Note the effect on the potential.

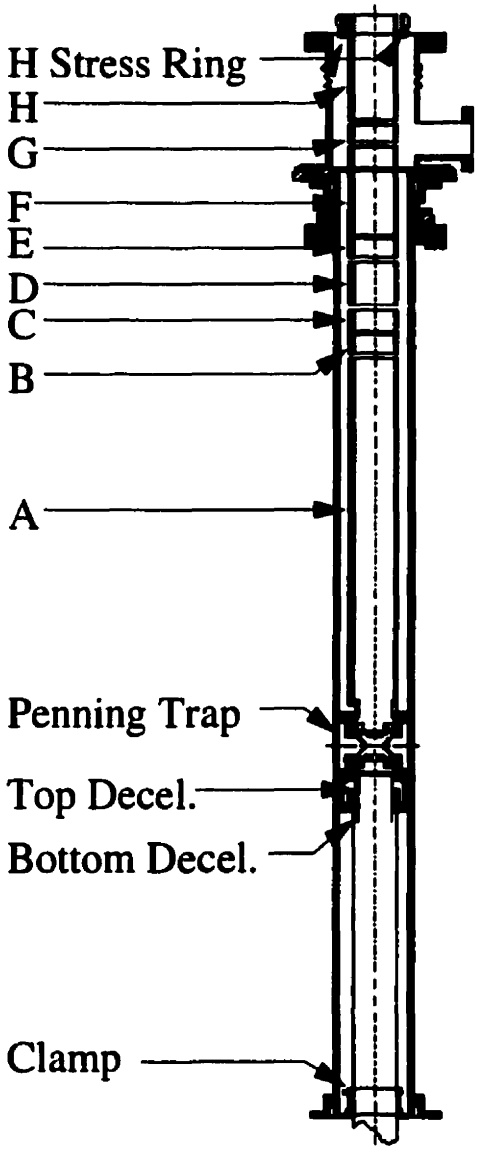

Figure 3.11: Magnet chamber.

Electrodes before entering the Penning trap.

The Penning trap, like the Paul trap, is made of a ring and two endcaps. However here the ring electrode is divided into four sectors, used to produce the RF potentials needed to excite the cyclotron motions. Its characteristic distance is $z_o = 8.4mm$.

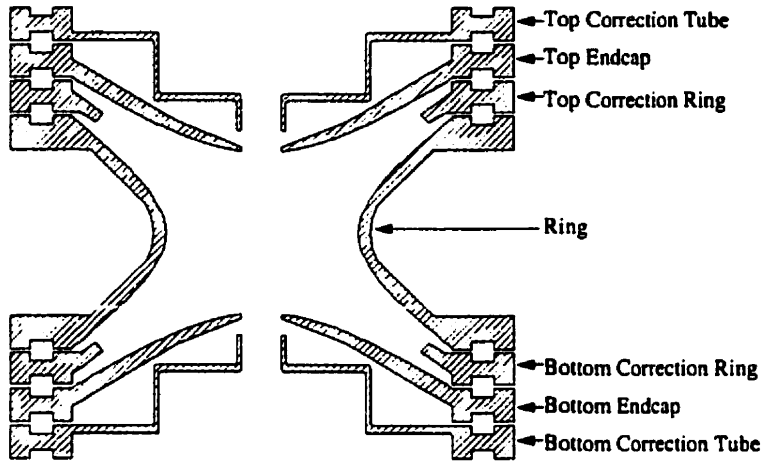

Figure 3.12: The Penning trap. Not shown in this cross section is the sectioning of the ring into four sectors.

Two Correction Rings are added to compensate for the effects of the finite size of the trap. on the quadrupole field. Furthermore, Correction Tubes are placed outside both the Bottom and the Top Endcap to reduce the effect of the field from neighboring drift tubes which leak through the holes in the endcap. With these correcting elements, the field inside the trap volume follows closer to the theoretical quadrupolar relation. This makes the potential inside look quadrupolar over a larger volume.

The capture scheme at the Penning trap is somewhat different from that of the Paul trap: in the case of the Paul trap, the incoming ions have a higher energy than the trap potential, so that a pulse is applied on the top endcap to slow down the ions to an energy lower than the trap well depth for capturing. In the case of the Penning trap, the incoming ions have an energy just above the potential of the ring electrode, whereas the endcaps are set at a higher potential —in our case, the ring was sitting at 0V, and the endcaps, at +5V. This meant that ions with energies between 0 and 5eV could be contained inside the trap. In order to capture, we apply a negative pulse on the bottom endcap, effectively opening the trap, and let ions enter. We then set the endcap back to its original potential, and the ions which are inside the trap are

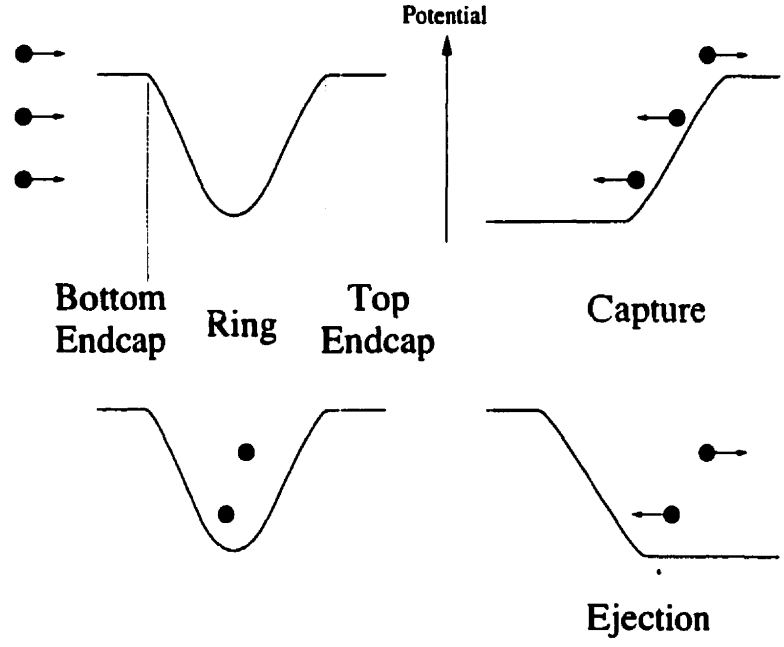

Figure 3.13: Capture and ejection schemes in the Penning trap. Note that only ions with energies between that of the endcaps and ring are captured.

confined. The trap has to be closed fast enough so that ions entering it won't have time to escape once they are reflected back. By keeping in mind that ω_z for gold ions in a 5V potential corresponds to about $5\mu s$ (see equation 2.8), we can open the trap during an appropriate time interval. For the ejection, we apply a negative pulse on the top endcap, and let the ions leave. This is shown schematically in figure 3.13.

We saw in section 2.4 that we need to apply a radial RF dipole driving field to excite the ω_+ and ω_- cyclotron motions of the ions inside the Penning trap, and that in order to do so, we could split the ring into halves. The ring in our setup is divided into quadrants, which enables one to set a quadrupolar radial field. In order to set the dipole field we desire, we simply tie the neighboring sectors two by two. We take the desired RF signal from a waveform generator and send it to one of the halves. The same signal is phase inverted and sent to the other half, thus creating the desired dipole field.

Appropriate voltages for the correction rings and tubes are found by observing average TOF vs. ω_D plots: deviations from equation 2.5 for an ideal quadrupolar electric field will yield plots which are distorted when compared with the one shown on figure 2.14. The electrodes are set at trial values, and are adjusted to make the curves as symmetric as possible.

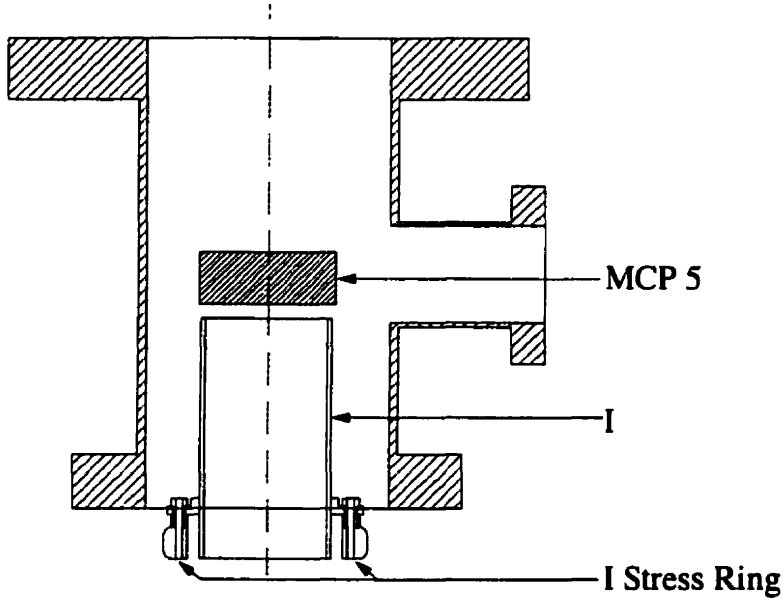

Figure 3.14: TOF chamber.

Ions ejected from the Penning trap then need to be slowly pulled away from the magnetic field, thus converting their cyclotron energy to axial kinetic energy, and accelerated toward the MCP5 for TOF detection. This is accomplished by the electrodes above the trap, as shown in figures 3.11 and 3.14. Electrode A was made very long so that ions would slowly drift through it and effectively convert their cyclotron energy to axial kinetic energy, yielding the so-called time-of-flight effect at MCP5. The rest of the electrodes are used to refocus the ion beam on MCP5. Typical potentials for the Penning trap and the surrounding electrodes are shown on table 3.4. Note that a vacuum valve also separates electrodes H and I, so that

another stress ring was used in that part of the setup.

3.6 The superconducting magnet: its mapping and adjustment

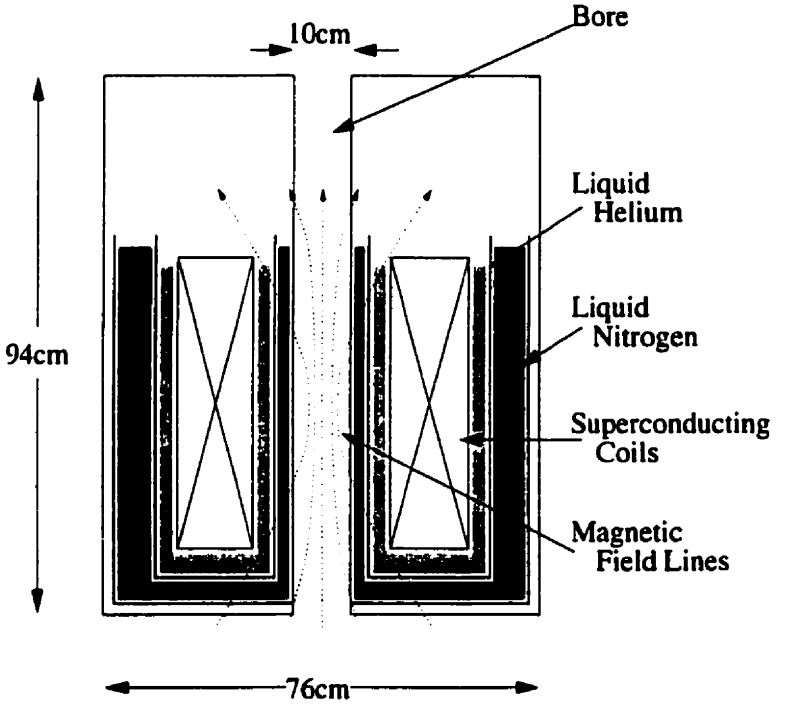

Figure 3.15: The superconducting magnet. It is cylindrically symmetric; the Penning trap sits at its center.

The superconducting magnet, custom made by NALORAC, was designed to produce a highly homogeneous 6T magnetic field over a volume of one cubic centimeter. A schematic diagram is shown in figure 3.15. It is 94cm tall, and has a hollow bore of 10cm diameter along its axis of symmetry. This is where the Penning trap and its associated injection and ejection electrodes sit. The magnet is made of superconducting coils which bathe in a liquid helium dewar, which is itself surrounded by

Electrode	Voltage (V)
Drift Tube	-2235
Bottom Deceleration	-2235
Top Deceleration	-10.00
Correction Tubes	+5.74
Endcaps	+5.00
Correction Rings	+2.25
Ring	0.00
A	-1.25
B	-300
C	-400
D	-650
E	-850
F	-1500
G	-700
H	-1500
H Stress Ring	-400
I	-1500

Table 3.4: Typical potentials in the Magnet Bore.

liquid nitrogen. There are two concentric main coils, and their joint condition of constant flux amounts to a 90% correction for outside perturbations at the center of the magnet. The stability in time is better than $\frac{dB}{dt} = 6 \times 10^{-9} Tesla/hour$. The magnet also contains nine superconducting correction coils, called *shims*, which provide fine tuning of the field at its center. They are made to correct the field in the z, z^2, z^3, x, y, xy, xz, yz, and $x^2 - y^2$ directions. The main coils are first powered up to set a field like the one shown in figure 2.12, then the shims are used to fine tune it to the desired homogeneity.

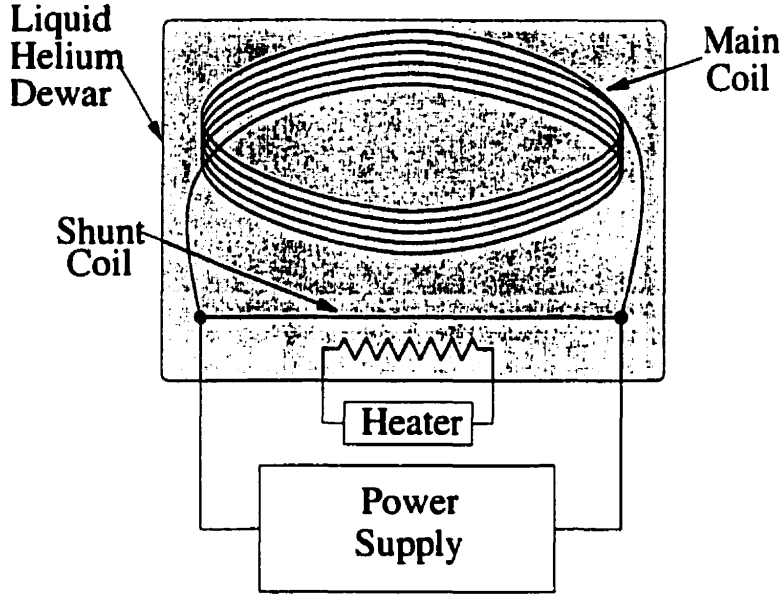

Figure 3.16: Electrical setup for powering up the superconducting magnet. The main coil and shunt are superconducting.

The circuitry involved in powering up the two main coils is shown in figure 3.16. There, we see a coil with its two leads (the setup is identical for both coils), and a shunt wire which completes the circuit. These wires are superconducting, and under normal operation, the current goes through them to produce the highly homogeneous magnetic field. In order to be able to supply current to the main coil, we need to bypass the shunt: this is done by heating it up, making it a normal conductor. The

current then goes through the main coil and the power supply, and we can adjust the current. When the desired setting is reached, the heater is turned off, making the shunt a superconductor again, and we can disconnect the power supply. The current will then pass through the shunt, resulting in a self-sustained mode of operation. Since the two coils in our setup are concentric, one has to raise current in each of them in small steps, alternating between one and the other. This is because raising the current (and therefore the flux) in one makes the current in the other drop.

Once the two main coils are powered up, we need to find the shim coil currents which will make the magnetic field most homogeneous at the center of the magnet bore. Like the two main coils, the shims have shunts which can be heated up to supply current to them externally. In order to find the optimal settings, we used a NMR probe to map the magnetic field: it was mounted on a stand which could be moved axially in steps of 1cm. Furthermore, the probe could be mounted at the center (along the axis of the magnet), or put 2cm off center, in any orientation. We first adjusted the z, z^2, and z^3 shims using readings along the axis of the magnet, and then used readings off the axis to find adequate settings for the other shims.

We assumed that, near the center of the magnet, changes in magnetic field ΔB were proportional to changes in current ΔI in each correction coil. So if a current I_i is set in the i'th coil, its effect on the field will be:

$$\Delta B_{ij} = \left(\frac{dB}{dI}\right)_{ij} I_i$$

We see that the field B at any point will be the field with no current in the coils, B_o, plus the contribution from each of the nine coils:

$$B_j = B_{oj} + \sum_{i=1}^{9} \left(\frac{dB}{dI}\right)_{ij} I_i.$$

This means that by taking readings at different points without current in the shims,

(x,y)(cm)	B(Tesla)($\pm 2 \times 10^{-6}$)
z = -0.5cm	
0,0	5.8895300
2,0	5.8891285
0,2	5.8891195
-2,0	5.8892109
0,-2	5.8890842
z = +0.5cm	
0,0	5.8895467
2,0	5.8896510
0,2	5.8893697
-2,0	5.8894393
0,-2	5.8896704

Table 3.5: Magnetic field readings near the center of the magnet (0,0,0).

we can get values for B_o. Then, by changing the current in each shim consecutively and again taking readings, we can find $\left(\frac{dB}{dI}\right)_{ij}$. We can then solve this equation and find the currents required to produce a homogeneous field. Although the assumption behind this method is not physically exact, we repeated the procedure many times and found that the field was becoming more and more homogeneous with every iteration. A problem occurred in that three of the shims are not functioning, and we had to carry out this procedure without the z, xz, and yz shims. Table 3.5 shows the last readings obtained, and the homogeneity is better than $\frac{dB}{B} = 1.25e{-}5$ over one cubic centimeter.

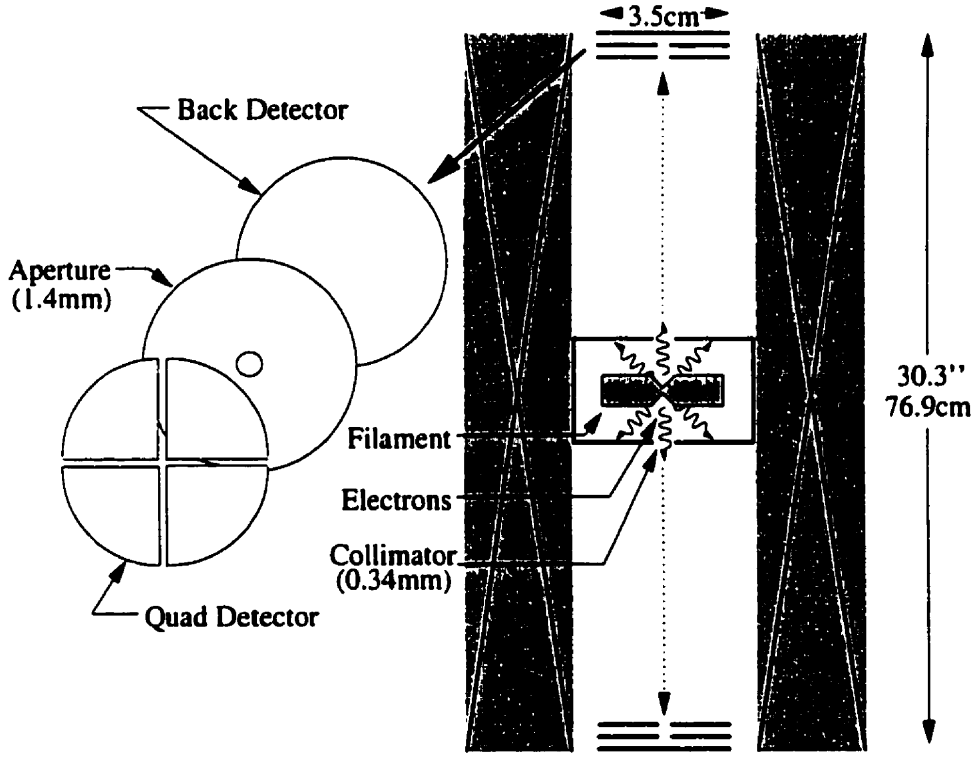

Figure 3.17: Alignment jig used for magnet bore alignment. We see the electron source and its collimators, along with the two sets of detectors, which are simply sheets of metal which we read the current on.

The hollow bore of the magnet, which is to house the Penning trap and TOF sec-

tion, contains a 7.6cm molybdenum cylinder in which all of the optics sit. It therefore needs to be very accurately aligned with the magnetic field. For its alignment, we send a collimated beam of electrons from the center of the bore towards both ends of the magnet and detect these electrons as they follow the magnetic field lines. If the tube is off center or its axis at an angle with respect to the magnet axis, the electrons reach the end of the magnet off its axis. Only when properly aligned will the electrons reach the ends of the magnet along the tube axis. For this purpose, an *alignment jig* was designed: it is made of an electron gun with collimators which sends two beams along opposite directions, and a set of detectors is placed at each end as is shown on figure 3.17. A sheet of rhenium was used as a filament, and the electron beam produced was collimated using two 0.34mm apertures to send beams upward and downward. The two detectors are identical; they are made of sheets of metal on which we read the current using a pico-ammeter. They have three layers of metal sheets: the first one seen by the beam is divided into quadrants, and gives us a position sensitive reading. It is followed by one electrode with a 1.4mm aperture and a solid disc.

In order to perform the alignment, the Mo tube is roughly centered, and the filament is heated up. We then take readings on the quad detectors and move the tube to center the beam. As the tube approaches the axis of the magnet, currents will appear on the apertures and back detectors, and these can be maximized. A heating current of $7A$ was sent through the filament, and it was biased with $50V.$ with respect to the collimator, which is kept at ground potential. This produced total currents of about $500pA$ on each set of detector. After about twenty adjustments, no current could be read on the quad sectors with the pico-ammeter, and about $400pA$ were seen on the back detectors. The adjustment was accurate to $0.2mrad$ in orientation, and 0.2mm in lateral position.

3.7 Optical alignment of the CPTMS

Once the molybdenum tube is aligned with the magnetic field, its axis defines the central line along which the ions have to travel, from the target to the TOF detector; the next step was therefore to align the rest of the electrodes with the Mo tube. In order to do this, we used nine apertures placed along the ion optical path and shone a HeNe laser from the top of the setup. The chambers were then moved (except for the magnet bore) until the laser beam could be observed on the target: this meant that all of the apertures were aligned with respect to the magnetic axis of the coil.

The CPTMS is separated into three groups of chambers which can be moved independently: the first part is from the sample wheel to the top of Lens 3, in the Cryo Chamber; the second is the top drift tube of the Cryo Chamber, and the third is from the Magnet Bore to the TOF Chamber. The movement is possible because of bellows above and below the Cryo Chamber —note that the bottom electrodes in it are fixed to the flange on the Lens Chamber, so that they move with the bottom group of electrodes. In order to optically align the system, one would ideally put two apertures in each of these groups. For the top one, we put a 1.5mm aperture on top of Electrode H. This, in combination with the 5mm apertures on the Penning trap endcaps and correction rings, defines a line which has to be matched by the other two groups. For the bottom group, another 1.5mm aperture was put on top of the drift tube below MCP4. This, along with Apertures 0 to 2 and the 3mm aperture of the ramping cavity, defined the line for the bottom group.

3.8 Experiment control and data acquisition

The first aspect of experiment control in our setup is vacuum. There are three issues to keep in mind in order to understand the vacuum system on the CPTMS: first,

Chamber	Pressure (torr)
Ionization	1.2×10^{-7}
RFQ	3.0×10^{-5}
Lens	8.3×10^{-8}
Cryo	8.4×10^{-9}
TOF	5.4×10^{-10}

Table 3.6: Typical pressure readings in the CPTMS. They range from about 1×10^{-7} torr in the Ionization chamber to 5×10^{-10} torr in the Magnet Bore.

ions need to travel in a clean, high vacuum environment in order not to be lost to collisions. Second, the Paul trap has to be operated under about $10^{-4} torr$ pressure for the cooling. Third, the Penning trap has to be operated under ultra-high vacuum ($< 10^{-9} torr$) in order for the energy transfers between captured ions and residual gas atoms to be negligible. The vacuum system was designed with this in mind; it is shown schematically in figure 3.18.

The main vacuum pumps are four turbo-molecular pumps TP1 to TP4, and a cryogenic pump, CP1. These are backed by four mechanical roughing pumps, P1 to P4, and another turbo-molecular pump, TP5. TP1, TP2, and TP3 pump on the Ionization Chamber, RFQ Chamber, and Lens Chamber, respectively. CP1 and TP4 are used to pump the bore of the magnet: since a pump can't be put at the Penning trap level, these were put to pump above and below it. Pressure readings are obtained from thermocouples (TC#) and penning ion gauges (I#). Typical readings are shown in table 3.6. We see that the system sustained pressures between 1×10^{-7}torr in the ionization chamber and 5×10^{-10}torr in the TOF chamber.

One crucial aspect to consider in setting up an ultra-high vacuum system is the choice of the materials used and their cleaning. Most of the parts of the CPTMS

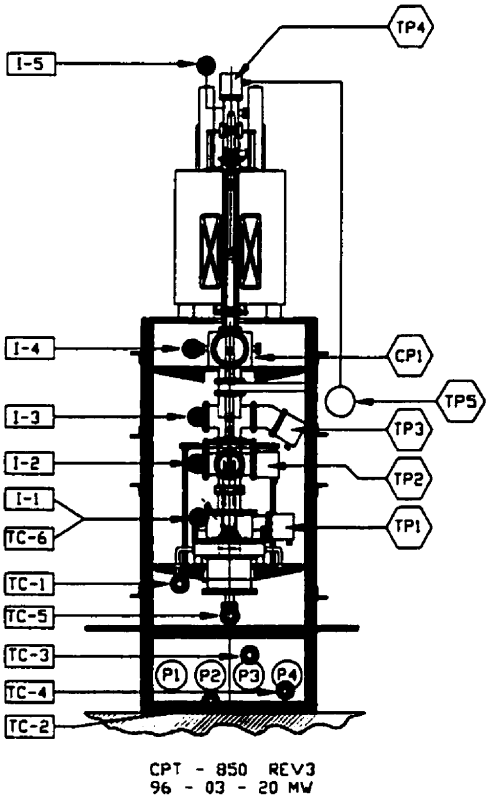

Figure 3.18: The vacuum system. I-#: ion gauge; TC-#: thermocouple; TP#: turbo-molecular pump; P#: roughing pump; CP1: cryogenic pump.

are made of stainless steel and oxygen-free copper. They were all thoroughly cleaned using electropolishing and appropriate etching. Another very important aspect of our vacuum system is its controls: pump status, pressure readings, cooling water

supply, and air pressure (for the valves) have to be constantly monitored in order to shut down the system in a non-destructive way in case of any failure. A computer does the monitoring and reacts appropriately in case of such an event. Then, all high voltages are turned off, valves are closed, and pumps are shut down (except for CP1, which is isolated through a valve). High purity dry nitrogen gas also is introduced in the system so that air from outside won't infiltrate the chambers. In this way, the vacuum system can be turned on and pumped down to the readings shown in table 3.6 in a few hours, even after having been shut down for many days.

Another aspect of experiment control is the voltages to be supplied to all the electrodes on the system. The voltage supplies needed to operate the CPTMS can be divided into five categories: high precision DC voltages for the Penning trap, RF for the two traps, switching for the capture and ejection pulses, ramping for the cavity, and high voltage for the rest of the electrodes.

For the high voltages, a LeCroy high voltage power supply was used. It could be programmed to ramp voltages on all its outputs at the desired rate up to to the final settings. It also possesses an input for emergency shut down, which was supplied by the vacuum control computer. The ramping cavity also needs to have a high voltage to be applied to it; to this end, an arbitrary waveform generator's output was sent to a fast amplifier. In this way, the 100V/μs ramp could be sent to it. For the capture and ejection pulses on the Penning trap, we needed pulses of a few volts to be added on top of the DC on the endcaps, as described in section 3.5. We used arbitrary waveform generators and programmed the desired signals; their outputs were capacitively coupled to the appropriate endcaps. Capture and ejection pulses on the Paul trap were discussed in section 3.3. For these, we needed pulses of a few hundred volts to be applied on the endcaps. For this, fast switches were custom-made, and high voltages needed were supplied by the LeCroy unit. The RF for the penning trap had to be a few tens of millivolts: for this, a waveform generator's output was

sent through an attenuator. For the dipole excitation, the output was split in two: one signal was sent to one half of the ring electrode, and the other was phase inverted and sent to the other half. For the Paul trap, where a few hundred volts RF had to be used, a waveform generator's output was sent to an amplifier. For the DC on the Penning trap, we needed voltages stable to part of a millivolt; for this, a high precision DC power supply was used. It used two highly stable power supplies as positive and negative reference voltages, and potentiometers to set the outputs at intermediate values.

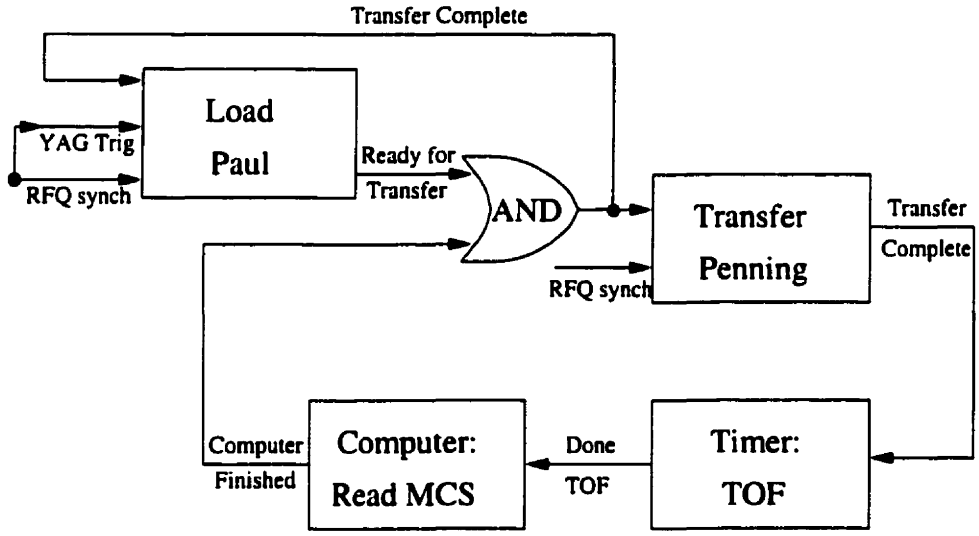

Figure 3.19: Main timing diagram.

Timing and data acquisition are done using a CAMAC crate coupled to a VMS computer through a SCSI port. In order to understand the role of these components, let us go through a mass measurement process; the main logic is shown in figure 3.19. We see that the Nd:YAG laser trigger and a synchronization signal from the RF on the Paul trap are used to trigger the capture pulse in the Paul trap. When the desired number of pulses is accumulated, the system is ready to transfer ions to the Penning trap. Ions are ejected from the Paul trap at a certain RF phase, and a signal is sent to trigger the capture pulse on the Penning trap. The ions are captured and

exposed to the RF for a certain time, and then a signal is sent for them to be ejected, and for the multi-channel scaler (MCS) to read the number of counts on MCP5 as a function of time and obtain a TOF spectrum. Once this is done, this data is sent to a computer to be written to tape, the computer updates the driving frequency to be applied on the Penning trap ring, and a signal is sent saying that the Penning trap is ready for the next capture.

The whole cycle is timed in function of the RF on the Paul trap. This is because injection and ejection are strongly affected by RF phase. We used an RF of 350kHz, corresponding to a period of $2.9\mu s$. The lamp inside the Nd:YAG laser was triggered at 20Hz, or every 50ms. 5μs after each pulse, the Q switch is fired at a certain phase with the RF (the laser output is maximum when the Q switch comes 5μs after the lamp flash). This signal is delayed to trigger the capture pulse on the Paul trap. This operation is repeated for as many pulses as we want to accumulate, and a signal is then sent for the ions to be ejected.

Once the computer has finished reading the MCS for the previous ion bunch, an ejection pulse is sent to the Paul trap at a certain RF phase. This pulse is delayed to initiate the correction voltage in the ramping cavity and later to generate the capture pulse on the Penning trap to capture the ions there. An RF signal is applied to the Penning trap and after the desired excitation time, the ions are ejected and the MCS is triggered. The scaler counts the number of ions arriving at MCP5 in time bins of $1\mu s$, and goes through 256 bins. This is the TOF spectrum which we use to find an average TOF for the current ion bunch. At this point, the MCS sends a look-at-me (LAM) signal to the computer which reads the spectrum and writes it to tape. Once the computer is finished, the RF driving frequency on the Penning trap is incremented, and a signal is sent to signify that the next ion bunch can be sent to it.

The computer is therefore responsible for reading the MCS and changing the

driving frequency. The rest of the logic is done by the CAMAC crate, although the computer is used to set and change all of the delays in the timing, and define the arbitrary waveforms. To this end, the computer uses a Fortran program to read a file which contains editable parameters for the run: timing for all the signals, frequencies for excitation in the Penning trap, arbitrary waveforms, number of cycles, and frequency increments. The system was designed to be able to switch from one species to another without being physically present in the room where the CPTMS sits: one simply needs to access this file, called *CONTROL.PAR*. The program used for data acquisition and timing, *TrapDAQ*, is coupled to a data analysis program, *TrapAnal*, through a graphical user interface (GUI): *TrapDisp*. It uses the OpenGL library to produce windows for displaying of the data and spectra obtained, as well as control of the run parameters. The data read is written to a magnetic tape drive.

Since the tests on the Paul trap involved the analysis of signals from the oscilloscope, a program was written to read the traces saved on floppies by the LeCroy scope. In this way, the results of the tests on the RFQ trap were obtained.

Chapter 4

Experimental results

We now present the experiments conducted in order to test the three main systems of the CPTMS: the laser desorption ion source, the Paul trap, and the Penning trap. We determined that the ion source could produce a stable gold signal which could be sent to the Paul trap. In the Paul trap, we captured, cooled, and ejected ions. Operating parameters were varied in order to find the optimal operating conditions. Multiple-pulse accumulation was performed. Note that no mention of this has been found in the literature, which makes this a premiere. At the Penning trap level, ions were captured and resonantly excited around the modified cyclotron frequency ω_+, yielding an average time-of-flight (TOF) vs driving frequency (ω_D) spectrum showing the expected minimum at ω_+.

4.1 Laser Desorption

The laser desorption ion source consists of a pulsed Nd:YAG laser shone on a gold target. Some of the ablated gold is given off as singly charged cations. These are accelerated toward a micro-channel plate detector, MCP1, for detection: a TOF spectrum is obtained. This is shown in figure 4.1: it shows printouts of the LeCroy

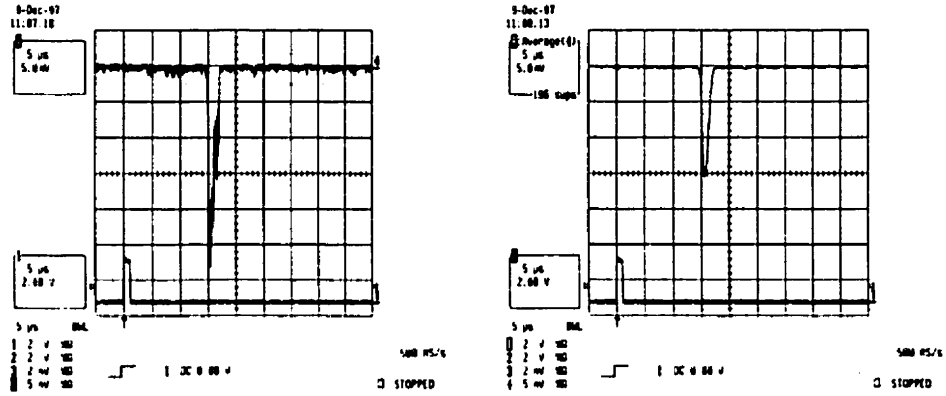

Figure 4.1: Gold signal on MCP1. A single pulse is shown (left), along with an average (right). The bottom traces are the laser firing (Q) switch.

oscilloscope traces obtained by reading the signal on MCP1. The bottom traces show the laser firing trigger, called the *Q switch*. On the top left, we see a gold signal coming about $15\mu s$ after the firing. On the right, we show an average signal. We can see a small RF signal superimposed on top of the gold signal: this is pickup from the RF on the Paul trap, which is at $350kHz$, or about $3\mu s$.

The 5ns pulsed laser was used at a repetition rate of $20Hz$. We used its frequency doubled beam of 532nm (the laser contains a crystal for this purpose). This higher frequency was more desirable than the 1064nm one because it is visible. Also, even though a lot of power is lost in the frequency doubling, the output was enough for our purpose. The laser beam was focused and centered on the target, and then its intensity was varied using a polarizer until a stable gold signal could be observed on MCP1.The most stable signals were obtained using about $6.0mJ$ per pulse. The ion yield between firings then varied by less than 25% of its average value, and was stable in time to less than $25ns$.

In order to estimate the ion yield, we looked at single ion pulses on the detector and averaged many such signals to find the mean integrated signal given by the detector for one ion. it was found that single ion pulses on MCP1 gave an average

time-integrated signal of $(3.4 \pm 0.3) \times 10^{-11} Vs$. With this, we looked at the average signal shown in figure 4.1 and found that about 1000 gold ions were detected. It was found that if the laser was stopped for more than a few tenths of a second, the ion yield dropped dramatically until a few uninterrupted laser pulses had been fired. The explanation we found is that while the laser is not firing, the target cools down. When it is turned back on, the energy deposited by the first few pulses is used to heat up the target back to an equilibrium temperature.

4.2 The Paul trap

The Paul trap in our setup is used to prepare the ions for the mass measurement in the Penning trap and make it more precise and effective. It does so in three ways: first, it cools down the ions. Second, it sends them as a monoenergetic bunch toward the Penning trap. Most importantly, it accumulates many ion pulses. This last feature is specific to our trap. It is very important because the CPTMS was designed to accept ions from an external source like a particle accelerator. Since ion yields can be very low, it becomes essential in a mass measurement process to accumulate many ion pulses before going to the Penning trap. In order to test the Paul trap, we first captured single pulses of ions. Then, the operating parameters were varied in order to find optimal capture conditions. Finally, for the first time in recorded history, multiple-bunch accumulation was observed in the Paul trap.

4.2.1 Trapping

In order to assess that the Paul trap could capture ions, we removed MCP1 and sent ions straight through the trap, detecting them with MCP2. The Paul trap was driven with an $800 V_{pp}$ RF between the ring and endcaps. The output is shown in figure 4.2.

We see the Q switch along with the Au signal right below, 21μs later. The bottom trace shows an average signal; it is time-delayed for clarity.

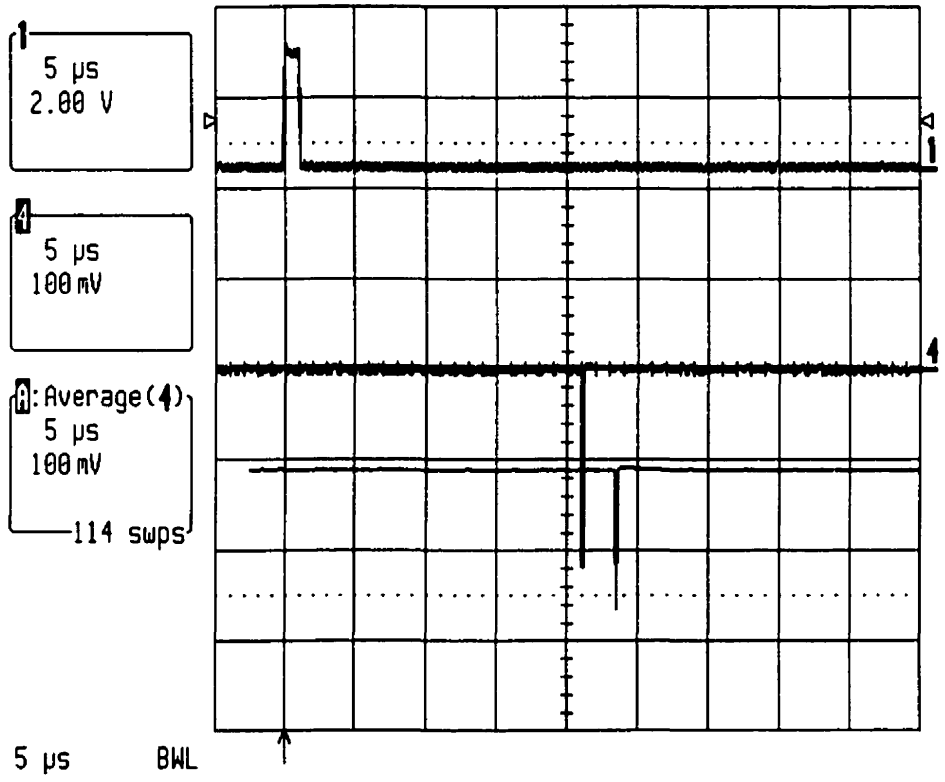

Figure 4.2: MCP2 signal for ions going through the Paul trap. The top trace shows the Q switch, and the bottom ones show the signal on MCP2: the actual signal, along with an average, which is offset in time for clarity.

The ion pulse is shorter in time than the one on MCP1: this is because of the RF in the trap, which slows down the first ions and speeds up the later ones. The phase at which the ions reach the trap affects the transmission, which is understandable, since the ions start at the sample wheel at a potential of -285V and reach the Paul trap which is sitting at -310V. The RF of $\pm$400V can either accelerate the ions or reflect them back, depending on its phase.

In order to capture ions, a capture pulse of +100V was applied to the top endcap,

and after a few microseconds, an ejection pulse was applied (+100V on the bottom endcap, -100V on the top one), as described in section 2.2. In order to time the capture pulse and RF phase correctly, the signal on MCP2 was observed: these two parameters were varied until the signal seen in figure 4.2 was reduced. This is shown in figure 4.3.

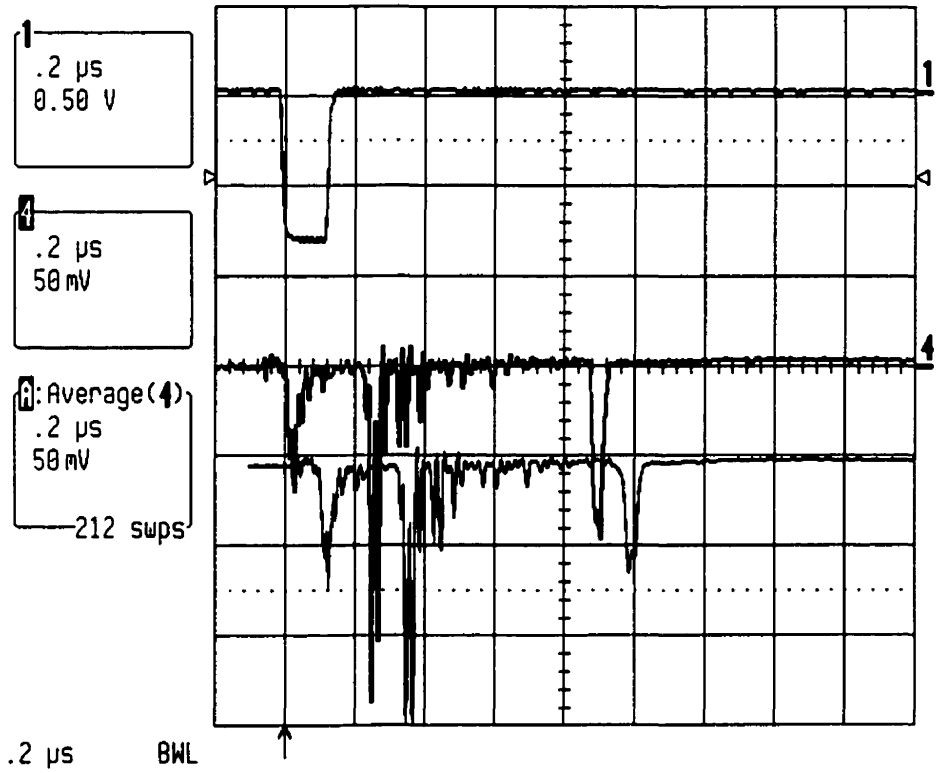

Figure 4.3: MCP2 signal for single ion pulse capture in the Paul trap. We see, at the top, the capture pulse, and at the bottom, the MCP2 signal and its average. Notice the pickup from the capture pulse.

At the top of the figure, we see the capture pulse, and the MCP2 signal right below. Once again, an average is shown, offset in time. The signal shows three pulses; the first two are pickups from the capture pulse, and the third one is the Au signal. This could be checked by blocking the laser: the third pulse would disappear,

but the other two would remain until the ejection pulses were turned off. Comparing with the trace in figure 4.2, we see that the signal has decreased by about 60%, which means that ions have either been reflected back, or captured in the Paul trap. By triggering the scope on the ejection pulse, we could find a signal on MCP2 from the ejected ions, and vary the parameters to improve the signal. This signal is shown in figure 4.4.

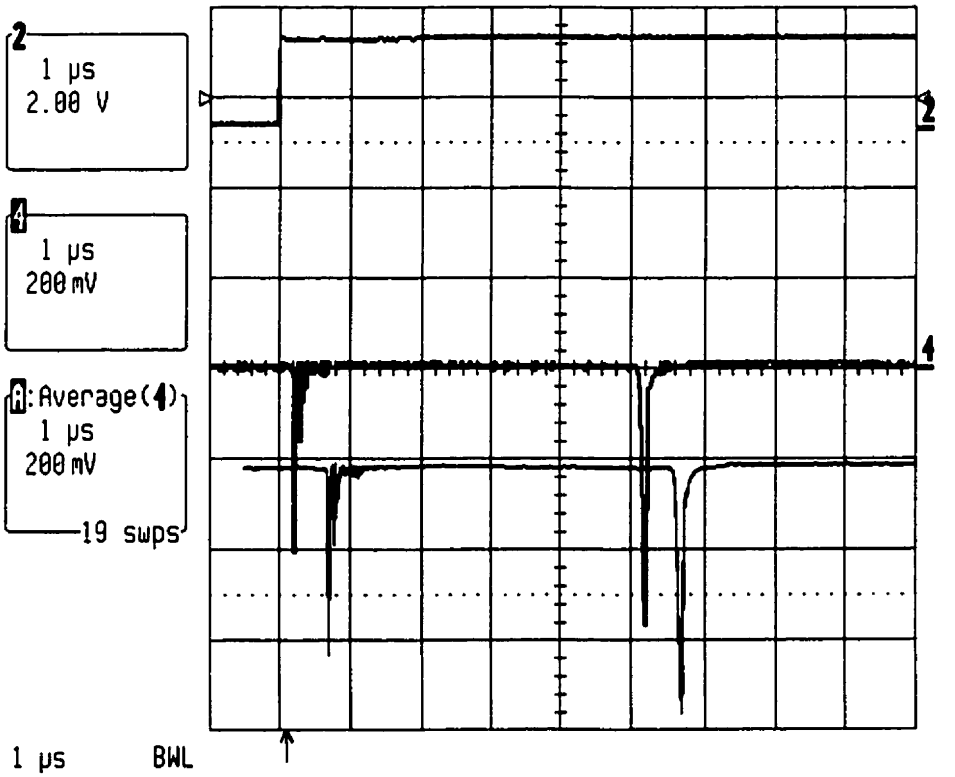

Figure 4.4: MCP2 signal for single pulse ejection in the Paul trap. We see, at the top, the ejection pulse, and at the bottom, the MCP2 signal and its average. Again, there is pickup from the ejection pulse.

Once again, the top trace shows the ejection pulse, and the the bottom two show the signal on MCP2 and its average. We see two signals: pickup from the ejection pulse, and the Au signal. The ejection pulse was made very long so that it wouldn't

RF amplitude	$800Vpp$
RF frequency	$350000.00Hz$
DC potential	$+25V$
Gas pressure	$2 \times 10^{-3}T$
Capture pulse	$100V$
Ejection (bottom)	$100V$
Ejection (top)	$-100V$
Capture pulse width	$10ms$
Cooling time	$20ms$

Table 4.1: Operating parameters for single pulse capture in Paul trap.

interfere with the ejected ions: it was found that if the pulse was very short, its falling edge would change the energy distribution of the ions. Table 4.1 shows the settings which were used for the aforementioned experiments.

4.2.2 Multiple bunch accumulation

Once single pulse capture and ejection were achieved, we tried to accumulate many ion pulses before ejecting them; it was found that the number of ejected ions was reduced as bunches were accumulated. This meant that one or many of the operating parameters had to be adjusted. There are many such parameters: the phase of the capture and ejection, the pulses height, their width, the cooling time, the buffer gas pressure. Which ones are crucial for accumulation? A closer look at figure 2.15 gives us the answer: the capture pulse has to be applied in such a way that the ions which are already in the trap won't escape. This means that the pulse has to be of low magnitude, and that it has to be as short as possible. It was found experimentally that the width of the capture pulse was a crucial parameter: once it was made about

300ns wide, accumulation became possible. This is shown in figure 4.5

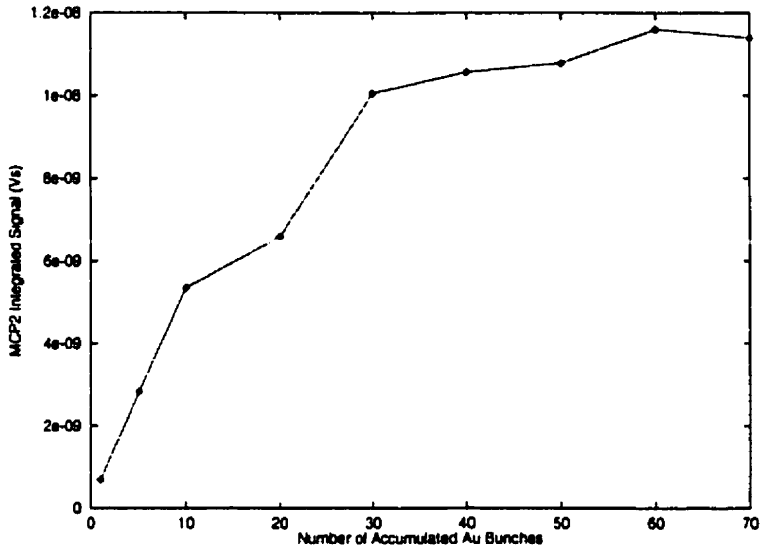

Figure 4.5: MCP2 integrated signal as a function of number of accumulated ion pulses.

What is shown is the integrated signal on MCP2, which is proportional to the number of ions detected. We can see that the signal grows linearly for the first few accumulated bunches, and then plateaus. There can be two causes for this: first, after a certain number of ions have been accumulated, the space-charge repulsion between them prevent more ions from being captured: the extra ions end up far from the center of the trap, and are lost because the field there is inadequate for capture. The other reason can be that since there is an aperture on the endcap, only part of the captured ions can be ejected. In this way, even if more ions are present in the trap, there is always the same number of ions (those close to the center) which are ejected and detected.

4.2.3 Variation of parameters

The different operating parameters of the Paul trap were varied. This was done in order to find optimal conditions for capture, accumulation, cooling, and ejection. In

these trials, five ion bunches were accumulated in the Paul trap for each measurement.

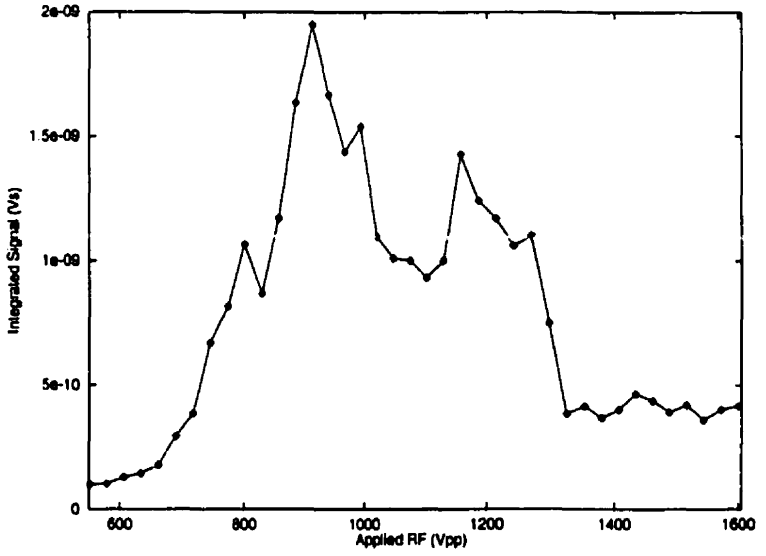

Figure 4.6: MCP2 integrated signal as a function of RF amplitude.

First, the amplitude of the RF bias was varied; the outcome is shown in figure 4.6. This does not give us a dependence on the RF per se, as the circuit which delivered it had a sharp resonance around 350kHz. This means that as the frequency was changed, the amplitude of the RF was also changed. The RF was varied between $500Vpp$ and $1600Vpp$. Then, we found the time required for individual bunches to be cooled down: the results are shown in figure 4.7. We see that the detected signal increases until about 8ms of cooling. This is because energetic ions will describe larger orbits in the trap, and therefore won't make it through the endcap aperture once they are ejected. After they have been cooled down, they are closer to the center of the trap, and can be ejected properly. This means that even when accumulating many bunches of ions, there should be an 8ms delay between the last capture pulse and the ejection pulse.

Multiple-bunch accumulation is useful as long as the ions which are captured in the Paul trap can be kept in it while other bunches are captured. We investigated

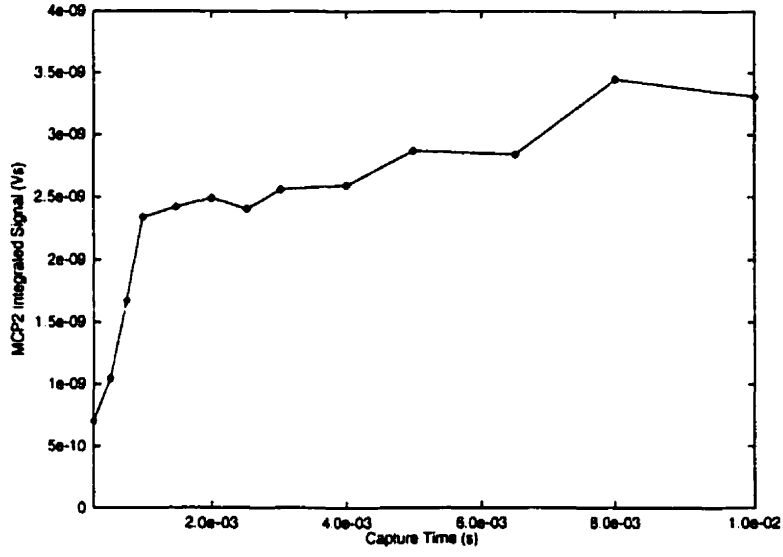

Figure 4.7: MCP2 integrated signal as a function of cooling time.

the time during which ions could be kept inside our trap. In other such devices, with no buffer gas, ions are kept for days. We kept the buffer gas on and looked at the Au signal as we delayed the ejection pulse; our results are shown in figure 4.8.

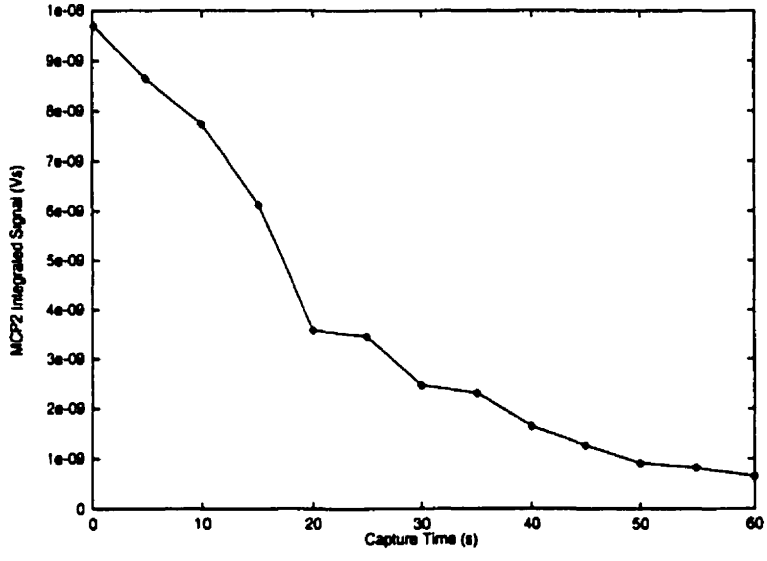

Figure 4.8: MCP2 integrated signal as a function of storing time.

We see that we lose 90% of the signal in about one minute. This is thought

to be caused mainly by impurities in the helium gas in the trap. As mentioned in the previous section, the width of the capture pulse is crucial in accumulation; we therefore varied it and observed the ejected Au signal. It was found that, for short enough capture pulse width, best accumulation corresponded to best single ion pulse capture. The results for five accumulated pulses are shown in figure 4.9. We see that there is a relatively narrow range of capture pulse widths (about 150ns, centered around 300ns) for which accumulation is possible. Once again, when the pulse is too narrow, ions don't have time to enter the trap. When the pulse is too long, ions which are already inside the trap have time to escape while it is open.

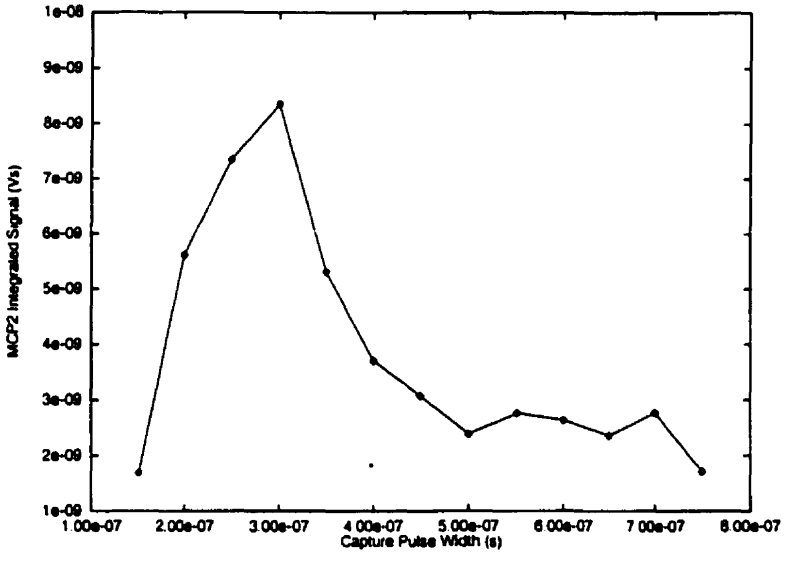

Figure 4.9: MCP2 integrated signal as a function of capture pulse width.

One problem which we encountered is that although simulations showed that the most monoenergetic pulse was to be obtained when ejected at zero phase with respect to the RF, all signal was lost around that phase. Figure 4.10 shows the output as a function of ejection phase: we see a peak around π. The exact cause for this discrepancy is not known, but it is thought to be caused by the coupling between the circuitry used to operate the Paul trap and the electrodes. Remember that a

resonant circuit is used to drive the trap, and that high voltage pulses are applied on top of this high voltage RF.

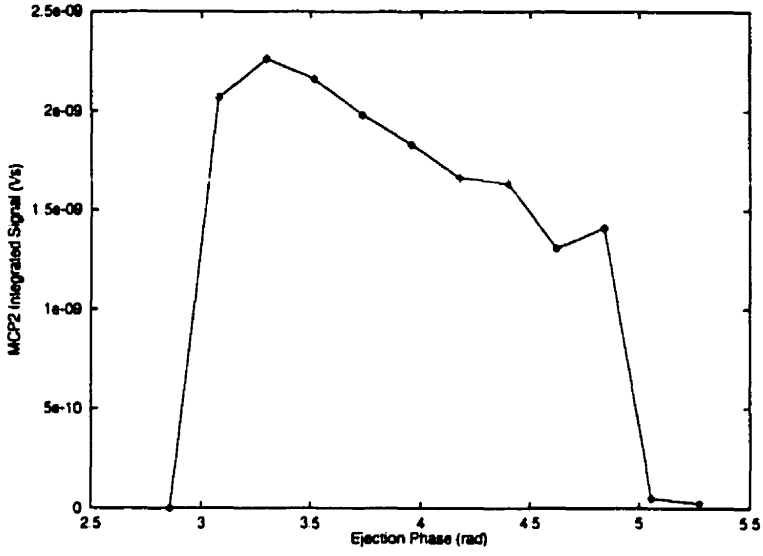

Figure 4.10: MCP2 signal as a function of ejection phase.

Finally, the buffer gas pressure was varied. In practice, we were limited by the turbopumps: it is unsafe to operate them above $10^{-4} torr$. We estimate that there is a factor of 10 difference between the pressure reading of $I2$ and the pressure inside the trap. The outcome is shown in figure 4.11

At low pressures, the signal is reduced. This is understandable, as a certain gas pressure is needed to cool down the ions in a given time. The fact that the signal is also lost at high pressures is again an indication that there are impurities in the helium. Another explanation is that at high pressure, the helium which is being pumped through the endcaps' apertures interferes with the capture and/or ejection of the ions, due to the large flow.

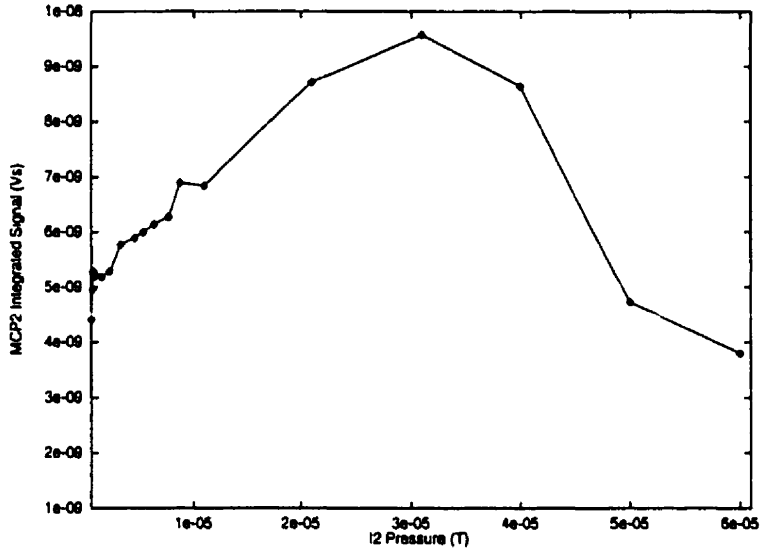

Figure 4.11: MCP2 signal as a function of buffer gas pressure.

4.3 The Penning trap

In order to assess that the Penning trap was functional, we first set its potential at drift and adjusted the lenses and steerers until we observed ions on MCP3, MCP4, and MCP5. Then, it was necessary to find the energy of the ions at the Penning trap level, so that its endcaps could be set at a higher potential to capture them. This was done by increasing the voltage on the bottom endcap until the signal on MCP5 was lost. After this, the potential on the ring was set 5V lower: this set the potential well depth in the trap. As described in section 3.5, the trap was opened by applying a -5V pulse on the bottom endcap. We know that ω_z has a period of about $10\mu s$ for our settings; the capture pulse was therefore made $5\mu s$ wide. By keeping the top endcap at ring potential and changing the timing of the capture pulse, we could detect the ions which were allowed in the trap: the ions which made it past the bottom endcap were detected on MCP5 as if all electrodes had been at drift. The top endcap's potential was then raised to its capture setting, and an ejection pulse was applied on it at a later time: Au ions could be observed on MCP5. This is shown in

figure 4.12.

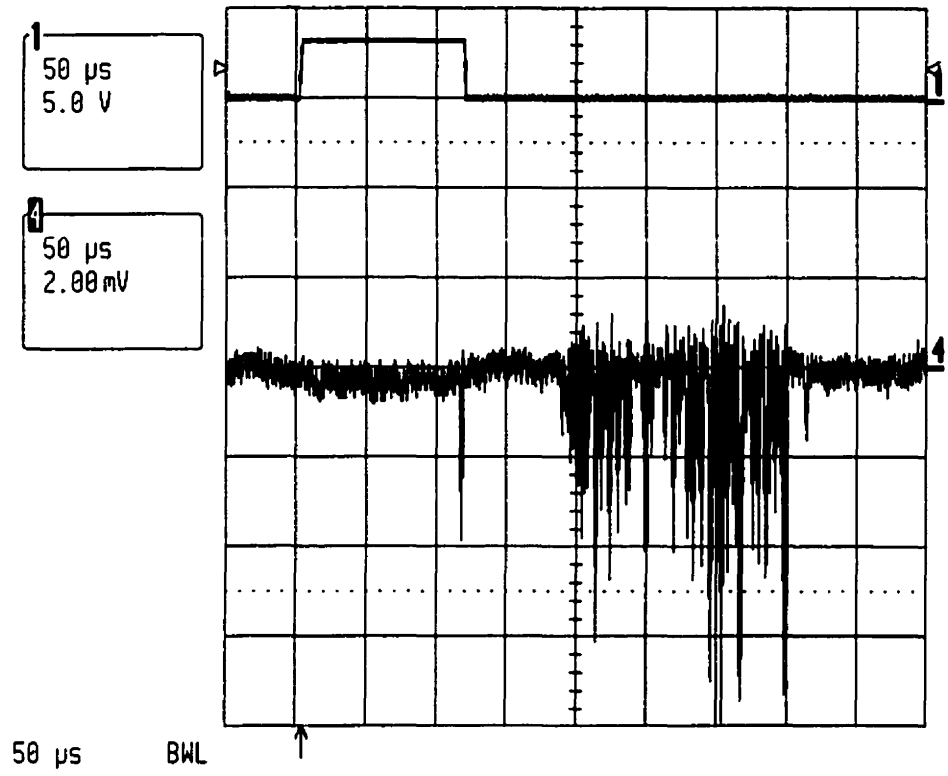

Figure 4.12: MCP5 signal showing ions ejected from the Penning trap. The top trace is the ejection signal, and the bottom one is the Au signal on MCP5.

This meant that ions were captured in the Penning trap. The capture time was increased to a few seconds with no change in the detected signal, so that it was deemed possible to apply a driving voltage. The first sign of resonance was observed by driving the ions around ω_+ with a dipole field of 1V. With such a high field, the ions undergo cyclotron motion of very large radii and are lost inside the trap. They collide with one of the trap's electrodes. We counted the number of ions ejected as a function of the driving frequency. In this way, a broad resonance was observed around ω_+. Once this frequency was found, it was possible to apply a proper driving voltage and observe the TOF effect. The RF amplitude was diminished to millivolts,

and the excitation time was set to 100ms. The correction rings and tubes were set to trial values: the rings were set to a voltage between that of the endcaps and that of the ring, and the tubes were set to a voltage a few volts lower than that of the endcaps. The first resonances observed were wider than the limit expected for a 100ms excitation. They were also not symmetrical. The RF amplitude and correction rings and tubes voltages were adjusted until a 10Hz, very symmetrical resonance was observed. The process was repeated for increasingly long excitation times, up to 1s. The resonance obtained is shown in figure 4.13. 2mV of RF were applied on the ring. The frequency increments are 0.25Hz.

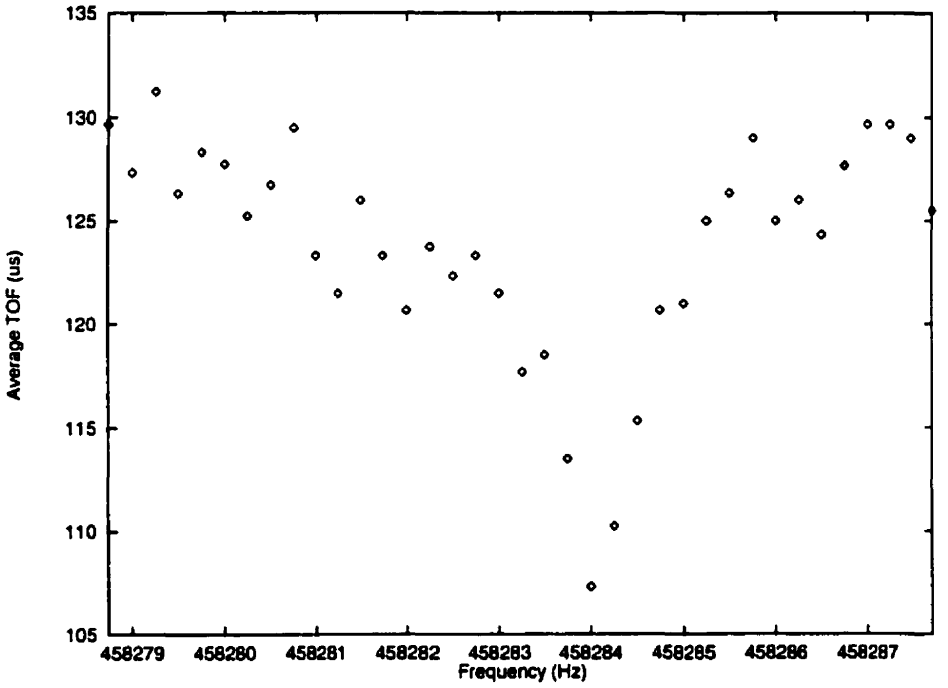

Figure 4.13: Resonance for ω_+. $25Hz$ increments, center around $458283.25Hz$.

We see that the FWHM is about 1Hz wide, which is the limit for a 1s excitation. It was found that the Au signal on MCP5 was lost after about 30 minutes, which is again thought to be caused by the Paul trap circuitry: slow drifts in the voltages applied on it will cause the energy of the extracted ions to vary. For a given Penning

trap potential, the trap only accepts ions in an energy range of ± 2.5V. A slight drift in RF amplitude, extraction phase, or extraction amplitude alters the axial energy.

Chapter 5

Discussion, Conclusion

The alignment of the superconducting magnet's molybdenum bore was done very accurately and effectively. The alignment jig proved to be an adequate tool, and experience from the previous year, when the method was developed and implemented, made the task almost a routine one. The method we used for the optical alignment of the whole system (sending a laser through a series of apertures through the whole ion optical path) gave an alignment which is good to a few millimeters. Although SIMION simulations show that the ion optical system was designed to compensate for this, we had to use different focusing conditions than the ones given by the simulations. The most probable cause is a misaligned electrode. The next time the system will be realigned, we should use a more precise method. For example, we could use crosshairs instead of apertures, and use a transit (the instrument used to survey buildings) to center each crosshair consecutively. Powering up and adjustment of the magnet was troublesome. As mentioned in section 3.6, three of the nine superconducting shims were not operational, which prevented us from obtaining the $\frac{\Delta B}{B} = 10^{-8}$ homogeneity over $1cm^3$ which the magnet was designed for. Although this had no impact on the experiments conducted for this thesis, this problem will have to be addressed before

doing mass measurements of higher accuracy. The average field in a $1cm^3$ volume at the center of the Penning trap is $5.889375 \pm 1 \times 10^{-6}$ Tesla.

The ion source was found to be very stable. Once adequate settings were found, the laser could be left on for a whole day without any change in the ion production. If it was turned off, say during the night, one would just turn it on in the morning and let it warm up for a few minutes and recover the gold signal. One problem is in adjusting the polarizer, prisms, and lens used to send an adequate beam to the target: everyone of these components is adjusted by hand, and any change has a big influence on the ion pulse created. Although it was found to be adequate for our experiments, one has to keep this in mind if another target is to be used. The other problem is caused by the data acquisition system: it takes many milliseconds for the computer to read the MCS, update the driving frequencies, and send the *Computer Finished* signal. Consequently, at high Paul trap ejection rates, the computer inhibits the Paul trap loading, which stops the laser Q switch (see figure 3.19). As we saw in section 4.1, this changes the ion yield for a few laser pulses. In order to operate the system at such high rates (less than 5 accumulated bunches between transfers) with a stable ion yield, it is necessary to bypass the computer signal.

The Paul trap is functional. It fulfills its purposes of capturing, cooling, accumulating, and ejecting ions. There now remains the task of characterizing it completely, comparing the results with theoretical predictions and simulations, and fixing the problems. One necessary improvement is to increase the range of applicable RF frequencies: presently, the range is only of a few kiloHertz, centered around 350kHz. If one wishes to capture light ions, we need to go above 1MHz and keep a constant voltage output. The reason why we wish to do this is that in order to get an absolute mass measurement, we don't want to use the absolute value of the magnetic field and plug it in equation 2.24, since we know that the field drifts (section 3.6). We would rather depend only on the fact that the field is homogeneous. We then get

the mass value by switching between a lighter species of known mass and that of the target species. Mass is obtained as a frequency difference between the two. In order to do this, we need to be able to change the frequency applied on the Paul trap. One problem which needs to be addressed is that of the drift in the energy of the ions ejected from the Paul trap. The energy drift could be caused by a slow drift in the capture and/or ejection phases, or on some voltage applied on the trap.

The Penning trap was shown to function, and a TOF effect was observed. Since the clock which advanced the MCS was counting at 1MHz, we could only count ions at MCP5 for $256\mu s$. With the voltage on Electrode A 1V below the top endcap's voltage, the time width in ion arrival was of the same order. By raising the potential on Electrode A, the TOF effect could be made better; for this, we need to get a slower clock.

Looking back at equation 2.28, we see that we can solve for the mass:

$$m = \frac{q}{2}\left(\frac{2z_o^2\omega_+ B - V}{z_o^2\omega_+^2}\right). \tag{5.1}$$

Using the numbers we have, we get $m_{Au} = 197.0 \pm 9 \times 10^{-4}u$. Comparing with the accepted value of $196.9665 \pm 1 \times 10^{-4}$ [27], we get an error of $\frac{\Delta m}{m} = 4 \times 10^{-4}$. There can be a few reasons for this discrepancy: first, the voltage on the Penning trap's electrodes, which can only be monitored to 0.01V. Then, the magnet: we have observed some frequency shifts while adequate trap voltages were being looked for. Finally, space charge. Up to two hundred ions were detected after ejection from the Penning trap. Such a large number of trapped ions causes frequency shifts, as some of the ions are pushed in the regions of the trap where the field is not quadrupolar [25]. For high precision mesaurements, it will become necessary to work with fewer ions.

The goal of this project was to reassemble the CPTMS, make a few adjustments

in the setup, and assess that its three systems —the laser desorption ion source, the Paul trap, and the Penning trap — had been designed properly and could function. We succeeded: in six months, the system went from a state where all the parts were in boxes to an operational state. The laser desorption ion source was ideal in testing the rest of the system, and will certainly be very useful in putting the CPTMS in a state where its limit in resolution and precision will be achieved. Whereas the ultimate goal is to do measurements on isotopes collected from the Enge, the laser ion source can still yield useful data, for example on the mercury isotopes. The main achievement with the Paul trap was multiple-pulse accumulation, which will become essential in experiments where the ion yield is very low. As for the Penning trap, the most important point is that cyclotron energy was effectively transformed into axial kinetic energy in Electrode A. Although the Penning trap was tuned for only a few days, TOF effects of the order of 15% were observed, and the Fourier limit of 2×10^{-6} was attained for a one second excitation time. Now remains the challenging task of fully characterizing the CPTMS and going from 10^{-6} to 10^{-9} precision. Modifications to the Paul trap power delivery are under way, and the Penning trap is being fine tuned. The apparatus is soon to be coupled to the ATLAS beam, announcing a multitude of new measurements.

Bibliography

[1] S. S. M. Wong, *Introductory Nuclear Physics* (Prentice Hall, New Jersey, 1990).

[2] K. Sharma *et al.*, The Canadian Penning Trap Mass Spectrometer (TRIUMF EEC Proposal).

[3] A. H. Wapstra, G. Audi, and R. Hoekstra, *Atomic Data and Nuclear Data Tables*, 39 ed., 1988.

[4] G. Savard *et al.*, A Canadian Penning Trap Mass Spectrometer (proposal).

[5] G. Rouleau, Ph.D. thesis, McGill University, Montréal, Canada, 1992.

[6] E. Hagberg *et al.*, in *Proceedings of AMCO-9/NFFS-6* (IOP, Bernkastel-Kues, 1993).

[7] H. E. Duckworth, R. C. Barber, and V. S. Venkatasubramanian, *Mass Spectroscopy*, 2nd ed. (Cambridge University Press, Cambridge, 1986).

[8] T. Otto *et al.* (unpublished).

[9] R. Decker *et al.*, Z. Phys. A Atoms and Nuclei **301**, 165 (1981).

[10] C. Thibault *et al.*, Phys. Rev. **C12**, 644 (1975).

[11] M. Epherre *et al.*, Phys. Rev. **C19**, 1504 (1979).

[12] X. G. Zhou *et al.*, Phys. Lett. **B 258**, 285 (1991).

[13] N. A. Orr *et al.*, Phys. Lett. **B 258**, 29 (1991).

[14] H. Stolzenberg *et al.*, Phys. Rev. Lett. **65**, 3104 (1990).

[15] S. Becker *et al.*, CERN EP89-126, 1989.

[16] H. J. Kluge, Hyperfine Interactions **74**, 287 (1992).

[17] F. Vedel and G. Werth, *Ion Trap Instrumentation*, Vol. II of *Practical Aspects of Ion Trap Mass Spectrometry* (CRC Press, Florida, 1995), Chap. 7.

[18] in *Proceedings of the Workshop on Traps for Antimatter and Radioactive Nuclei* (TRIUMF, B.C., 1993).

[19] D. Ghalambor, Ph.D. thesis, McGill University, Montréal, Canada, 1996.

[20] F. G. Major and H. G. Dehmelt, Phys. Rev. **170**, 91 (1968).

[21] J. D. Jackson, *Classical Electrodynamics* (John Wiley & Sons, New York, 1975).

[22] R. E. March and R. J. Hughes, *Quadrupole Storage Mass Spectrometry* (Wiley, New York, 1989).

[23] N. W. McLachlan, *Theory and Application of Mathieu Functions* (Oxford, Clarendon, 1947).

[24] L. S. Brown and G. Gabrielse, Rev. Mod. Phys. **58**, 239 (1986).

[25] G. Bollen, R. B. Moore, G. Savard, and H. Stolzenberg, J. Appl. Phys. **68**, 4355 (1990).

[26] D. A. Dahl, *SIMION 3D Version 6.0 User's Manual*, Idaho National Engineering Laboratory, Idaho Falls, 1995.

[27] *Particle Physics Booklet*, Particle Data Group, Berkeley, 1998.